Part 3. Voltage front perturbation effects

Les Renardières Group

Indexing terms: *Arcing, Breakdown and gas discharges, Gas discharges, Load and voltage regulation, Overvoltages*

Abstract: Withstand voltage ratings for air insulation are partly based on test data obtained with standard biexponential impulses. The importance of the time parameters of the test impulse, with the distinction between lightning (LI) and switching (SI) standard impulses, is well established. The paper (Part 3) describes tests on a 6 m rod-plane gap with stresses which depart substantially from the biexponential voltage-front. Results are presented of the effect on leader growth, propagating under a switching impulse of critical shape, of a superimposed voltage perturbation of either LI or SI shape. For either type of perturbation, the time at which it is applied is important. The LI perturbation could arrest a young leader or enhance the propagation of a more mature leader. The electrical and spatial response of the discharges to such fast voltage perturbations is described. For SI perturbations, the change in the voltage derivative dU/dt, caused by the perturbation, controls the rate of change of the leader growth, and will provide a useful parameter in the modelling of nonstandard impulse breakdown. For such modelling, the results also justify the useful simplification that the linear charge density of 50 μC/m of a developing leader is unchanged by either LI or SI perturbations.

1 Introduction

The important influence of the time to crest on breakdown voltage is well known for standard test impulses of double-exponential shape. Departures from this shape may just as fundamentally affect the leader and leader-corona growth in the gap, and may often better represent the surge shapes which arise in practice. The difficulty of generating such shapes in the test laboratory at very high voltages has limited the amount of work on nonstandard voltage fronts. The present double-impulse test programme offered the opportunity to extend the available knowledge in this area. To provide as wide a range of data as possible, the second impulse was designed to create either a rapid (LI) or slow (SI) perturbation to an already growing SI discharge. The impulse combinations used are given in Table 1, which cites the three types of voltage perturbation which were applied to the basic 240/9000 μs impulse. After the perturbation at time Δt, the total voltage applied to the gap is thus the sum of the instantaneous values of the two applied voltage magnitudes.

Table 1: Impulse combinations

Basic impulse		Voltage perturbation		
Crest U^+ kV	Shape μs	Crest U^- kV	Shape μs	Δt μs
+1530	240/9000	−800 to −1100	2/30	30 to 180
+1455	240/9000	−470 to −1200	100/1500	60, 120
+1668 to 2162	240/9000	+490	100/1500	60, 120

Section 2 will describe the results obtained with LI perturbation, and Section 3 those with the SI perturbation.

In the test programme, the electrical and optical measurements were particularly designed to analyse the effect of voltage perturbation on the leader propagation phase. The spectroscopic investigation was also included in this programme, as it was possible in this case to synchronise the leader reillumination with the spectral-analysis time-resolving equipment (Section 2).

Paper 4827A (S3) received 14th January 1986

For the author details see Paper 4825A, Double-impulse tests of long airgaps Part 1

2 Lightning impulse perturbations

2.1 Breakdown voltage and time-lag characteristics

In Fig. 1 the variation of the breakdown probability with the delay Δt is represented; the positive voltage is at the

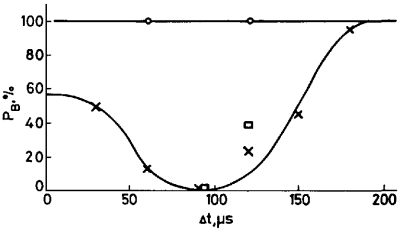

Fig. 1 *Probability P_B of breakdown*
Dependence on LI perturbation delay Δt
× 2/30 μs, −800 kV
○ 100/1500 μs, −800 kV
□ 2/30 μs, −1100 kV

constant level $U_{50} = 1530$ kV and the negative voltage is at $U^- = -800$ kV, or -1100 kV. For delays ranging from 0 to 90 μs the breakdown probability decreases from 50% down to 0%. Correspondingly, the average breakdown times (Fig. 2) do not vary appreciably before they become unmeasurable for $\Delta t = 90$ μs. At $\Delta t = 90$ μs, even if the negative voltage is raised above -1100 kV the breakdown probability remains zero.

For delays above 90 μs the breakdown probability

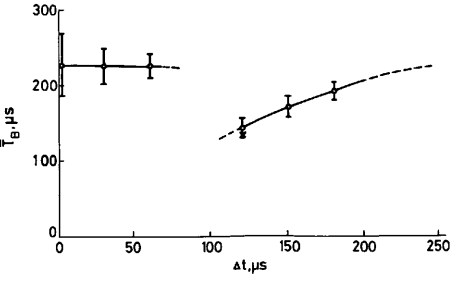

Fig. 2 *Time to breakdown*
Dependence on LI perturbation delay Δt

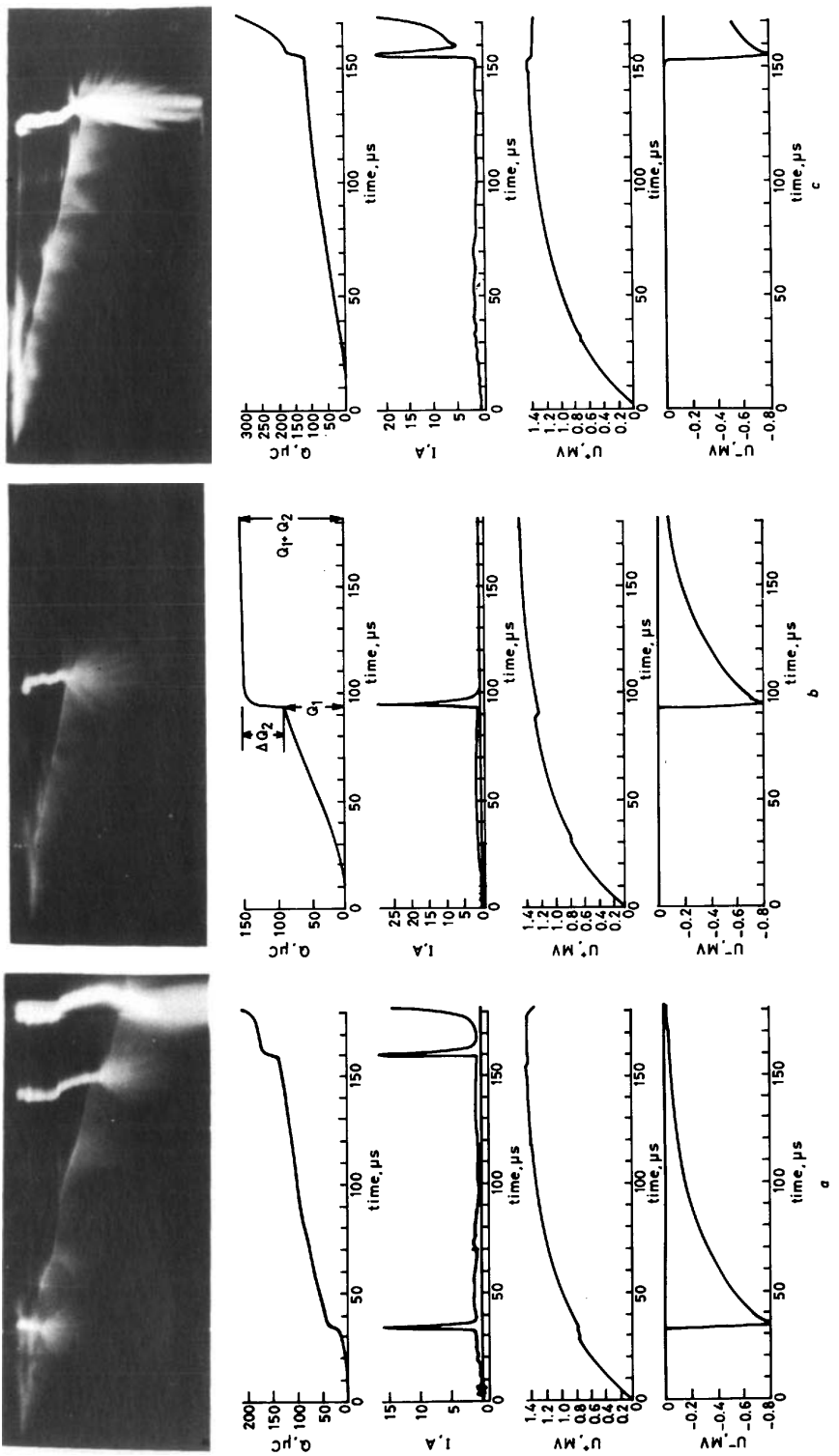

Fig. 3 *Test records of LI voltage perturbation effects*
(*a*) $\Delta t = 30$ μs; (*b*) $\Delta t = 90$ μs; (*c*) $\Delta t = 150$ μs
Row 1: Image convertor photograph
Row 2: Charge Q
Row 3: Current I
Row 4: Positive voltage U^+
Row 5: Negative perturbation voltage U^-

increases gradually again from 0 to 100%. The average breakdown times are in this case smaller than those for the original unperturbed gap; they increase slightly with Δt, and tend asymptotically to the original value. Three Δt regions may therefore be defined on the basis of the breakdown probability data:

(i) unperturbed region: $\Delta t \leqslant 60\ \mu s$

(ii) choking region: $\Delta t \simeq 90\ \mu s$

(iii) acceleration region: $\Delta t \geqslant 120\ \mu s$

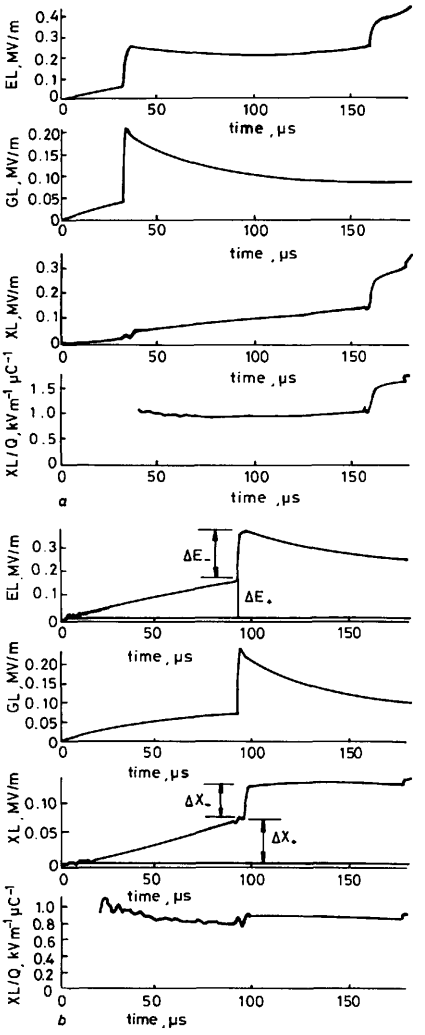

2.2 Transient records

The three regions referred to in Section 2.1 are clearly seen in Fig. 3. This gives synchronised examples of image-convertor photographs, charge, current and positive and negative applied voltages. In the case $\Delta t = 30\ \mu s$, the current and charge pulses which are associated with the voltage perturbation are not always accompanied by a change in the leader propagation, which remains continuous until the final-jump stage. The choking region associated with $\Delta t = 90\ \mu s$ is shown in Fig. 3*b*. When the voltage perturbation is applied, a large leader corona (i.e. from the leader tip) and channel reillumination occurs, and the leader propagation stops. The reason for the choking effect is seen in the current and charge records, which show a large injection of space charge in the corona region, following which the current extinguishes. Fig. 3*c* is an example of the acceleration stage when the voltage perturbation is applied at $\Delta t = 150\ \mu s$. In this case, the leader is so well developed that the large leader corona extends to the plane electrode. The final jump is launched and breakdown follows; closure of the shutter prevents fogging of the film. The charges Q_1, ΔQ_2 and Q_2 as defined in this Figure are used for quantitative analysis.

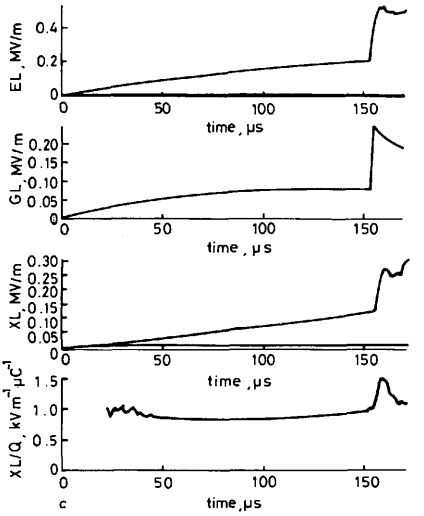

Fig. 4 *Electric field behaviour for LI voltage perturbation*
(*a*) $\Delta t = 30\ \mu s$; (*b*) $\Delta t = 90\ \mu s$; (*c*) $\Delta t = 150\ \mu s$
Row 1: Field, measured at probe *L*, *EL*
Row 2: Geometric field *GL*
Row 3: Space-charge field *XL*
Row 4: Field/charge ratio *XL/Q*

The electric field strength at the plane electrode was also recorded for the three régimes, and examples are given in Fig. 4. The records (*a*), (*b*) and (*c*) for $\Delta t = 30\ \mu s$, 90 μs and 150 μs, respectively, consist in rows 1 to 3, of the measured total electric field *EL* at the central probe *L* (see Part 1), and the geometrical and space-charge fields at this probe. The record of *XL* is obtained by digital subtraction from *EL* of the geometrical field *GL* at probe *L* created, in turn, by the two voltage impulses. The measured field changes $\Delta E+$ and $\Delta E-$ are also defined in this Figure. At $\Delta t = 30\ \mu s$, the space-charge field *XL* shows a step increased followed by a further gradual rise associated with the continued leader propagation. At $\Delta t = 90\ \mu s$, in contrast, no further rise occurs after the rapid stoppage of the leader. At $\Delta t = 150\ \mu s$, the step in *XL* is followed by a field decrease. This is the result of charge neutralisation by interaction of the leader corona with the plane before the final jump phase. For all Δt, the ratio *XL/Q* (row 4) is an indication of the proximity of the space charge to the plane.

Further information on current and total light output for $\Delta t = 90\ \mu s$ is given in Fig. 5. As described in Part 1, these represent the average values for 518 impulses applied during the spectroscopic studies. The optical record, obtained by the broadband photomultiplier/slit arrangement, shows a shape which resembles the current shape,

with the notable exception of an initial large spike following a rise time of about 200 ns.

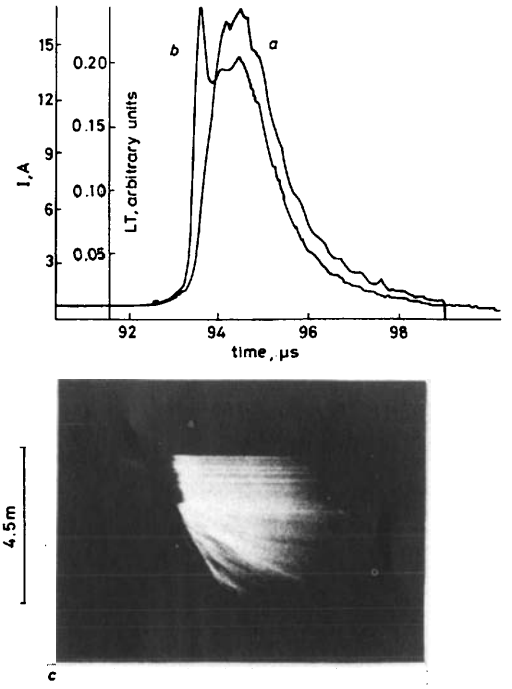

Fig. 5 *Fast time resolution records of LI perturbation effects*
a Current *I*
b Total light output *LT*
c Image convertor photograph

Also shown in Fig. 5 is an image-convertor record of high time resolution, which shows the result of the voltage perturbations on the leader channel and leader corona. The reillumination of the leader has a sharp front edge corresponding to the peak of the light emission. The corona streamer growth is also time-resolved sufficiently to indicate the propagation velocity of the order of 1 m/μs. The brighter region between the leader and its corona shows a brief phase of increased velocity of the leader tip caused by the voltage perturbation before its arrest.

This evidence thus indicates a two-stage process in the response of the discharge to the voltage perturbation. In the first stage, the low-current/high-light-output transient is representative of a voltage front propagation along the leader channel which results in an increase of the tip potential. The second stage ensues from the resulting leader corona: this acts as a current generator, and the light output and current then show a proportional relationship.

For slightly longer Δt of 120 μs and 150 μs, the choking effect of the perturbation is weakened and breakdown probability increases. Nevertheless, at $\Delta t = 120$ μs, Fig. 6 shows a leader-corona enhancement which is so vigorous that it traverses the 6 m gap. In normal circumstances this would inevitably result in breakdown of the gap, but here the space-charge effect is sufficiently large so as to prevent further leader growth and the onset of the final jump. The interaction of the leader corona with the plane electrode is shown to cause the electric field recorded at the plane to be reduced, suggesting that a charge neutralisation process occurs.

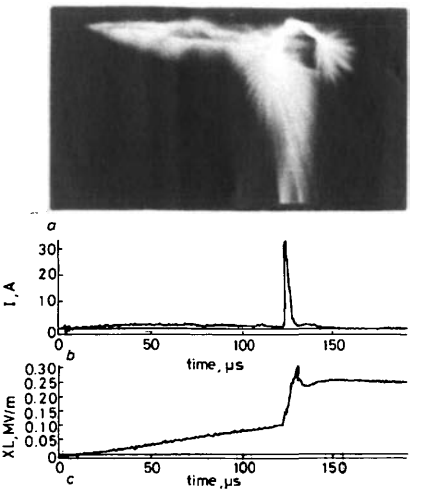

Fig. 6 *Corona perturbation*
Traversal of gap, current choking and space-charge field reduction
a Image convertor record
b Current *I*
c Space-charge field *XL*

2.3 Leader track analysis

A 3-dimensional analysis of the leader track on the basis of the digitisation of orthogonal static photographs has been carried out. This enables the spatial characteristics of the spark growth to be compared with the electrical transients. Fig. 7 gives an example of this work. Fig. 7*a* shows the track as seen from the static cameras. The track co-ordinates are recomputed so as to give the track profile as it would have been seen from the image-convertor position, in the absence of a streak sweep in the image convertor (Fig. 7*b*). It is then possible from the two tracks in Fig. 7*b*, for example, to reconstruct a framing sequence for the leader channel growth as in Fig. 7*c*. Thus the knowledge of the real 3-dimensional leader length and the true time-displacement of the image-convertor record can then be combined to give the real velocity of leader propagation. Fig. 7*f* and *g* give the real leader velocity and length for an example of the case $\Delta t = 30$ μs, together with the accompanying current and charge records. In this case, a small elongation of the real leader length can be seen following the voltage perturbation, and that the real velocity peak is an order of magnitude greater than the continuous propagation velocity.

2.4 Strioscopic measurements

The experimental technique of slit-aperture strioscopy with image-convertor axial-streak photography enables the effect of the voltage perturbation on the leader channel cross-section to be examined quantitatively by microdensitometer. Fig. 8 gives examples of such records and their analysis. The three régimes of Δt are again represented. In Fig. 8*a* at $\Delta t = 60$ μs the progressive leader expansion with time is clearly seen. Two shock waves are associated with this expansion. The first was generated near the leader tip shortly after inception. The second occurred following the voltage perturbation. A rapid expansion of the leader channel then took place which increased the area from about 4 to 6 mm^2. Fig. 8*b* shows a similar behaviour at

$\Delta t = 90$ μs. The existence of a second leader channel can also be seen here, below the expanding leader. No expansion occurs in this second channel, which indicates that no conduction is taking place. Fig. 8*c*, at $\Delta t = 150$ μs, shows a number of discontinuities. At about 130 μs, before the application of the voltage perturbation, a 'natural' restrike has occurred, accompanied by a shock wave and channel expansion. The resemblance between this effect and that which occurs following the controlled perturbation at $\Delta t = 150$ μs indicates that the 'natural' restrike may be a consequence of channel or leader-corona instability. Full breakdown occurred at about 180 μs. The photograph shows the strong shock wave and channel expansion which is a consequence of the large current peak.

2.5 Spectroscopic measurements

The spectroscopic characteristics of the leader channel, during the voltage perturbation at $\Delta t = 90$ μs, have been studied. The use of a slit to isolate the light from a small segment of the leader at 80 mm from the anode has enabled these characteristics to be time resolved. Fig. 9 shows such a record of the effect of the perturbation. The transient of Fig. 9*a* is the temporal resolution of the light output at a wavelength 337 nm. This may be directly compared here with the form of the total light ouput from the same section of the leader channel, which is shown in Fig. 9*b*. This clearly shows that the first peak of this total light is associated with a smaller spectral range than the remainder of the total-light transient. This has therefore been divided into two time régimes I (voltage front propagation) and II (corona and leader extension) for further study. Fig. 10 illustrates the full spectral range which has been recorded, respectively, during these two time régimes. In régime I the second positive system of N_2 is emitted strongly. Emission of the ionic spectrum of N^+ is also found. The atomic spectra of neutral N and O are almost absent. By contrast, in régime II, the N_2 second positive system is significantly weaker, probably because of molecular dissociation due to the temperature increase. This is confirmed by the appearance of the principal lines of atomic N and O and of H_α.

2.6 Charge and field characteristics

More than seventy impulses for the Δt range 30–150 μs were analysed to quantify the charge injection characteristics, and these results are illustrated in Fig. 11. The charge Q_1 is the average value of the total charge flow accompanying the positive discharge development up to the instant Δt. The increase in Q_1 with Δt is consistent with an average discharge current during the leader phase of about 0.8 A, with a slight fall in leader current after 100 μs. This may be associated with the falling slope of the applied voltage.

When the voltage perturbation is applied, a sudden charge injection ΔQ_2 occurs. The amplitude of the average value of ΔQ_2 increases continuously with Δt. This behaviour arises because of the more vigorous leader corona occurring from the more extensive leader growth.

Even for a well developed leader, the amplitude of the

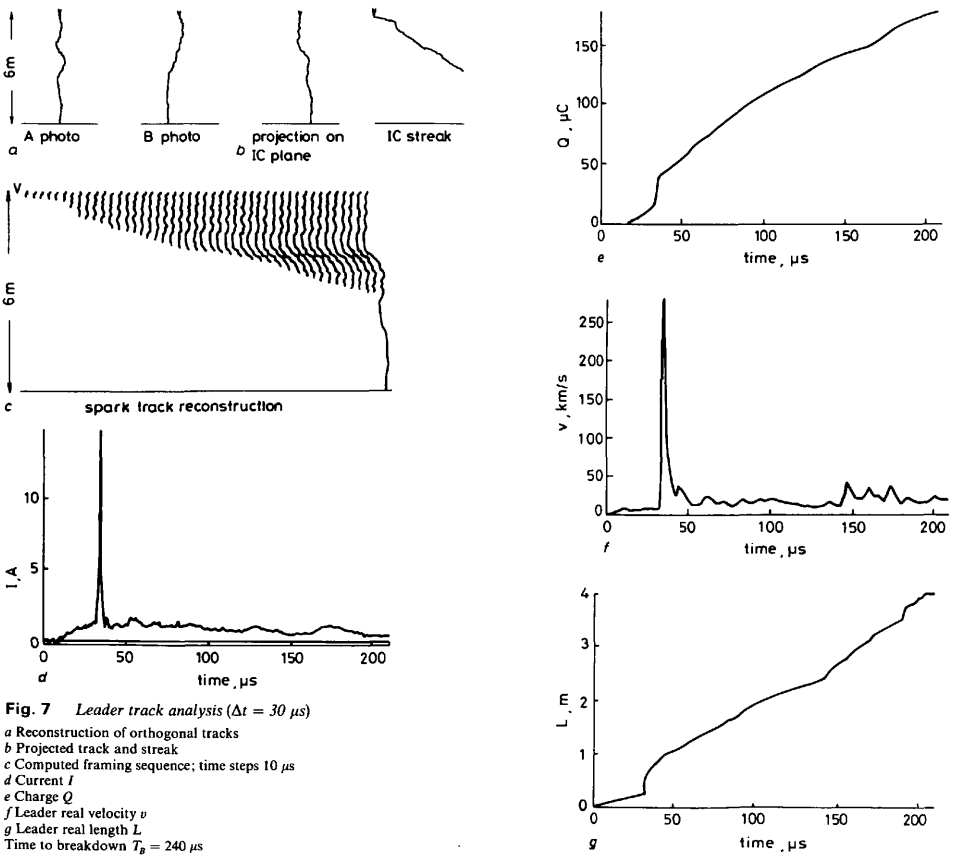

Fig. 7 *Leader track analysis* ($\Delta t = 30$ μs)
a Reconstruction of orthogonal tracks
b Projected track and streak
c Computed framing sequence; time steps 10 μs
d Current *I*
e Charge *Q*
f Leader real velocity *v*
g Leader real length *L*
Time to breakdown $T_B = 240$ μs

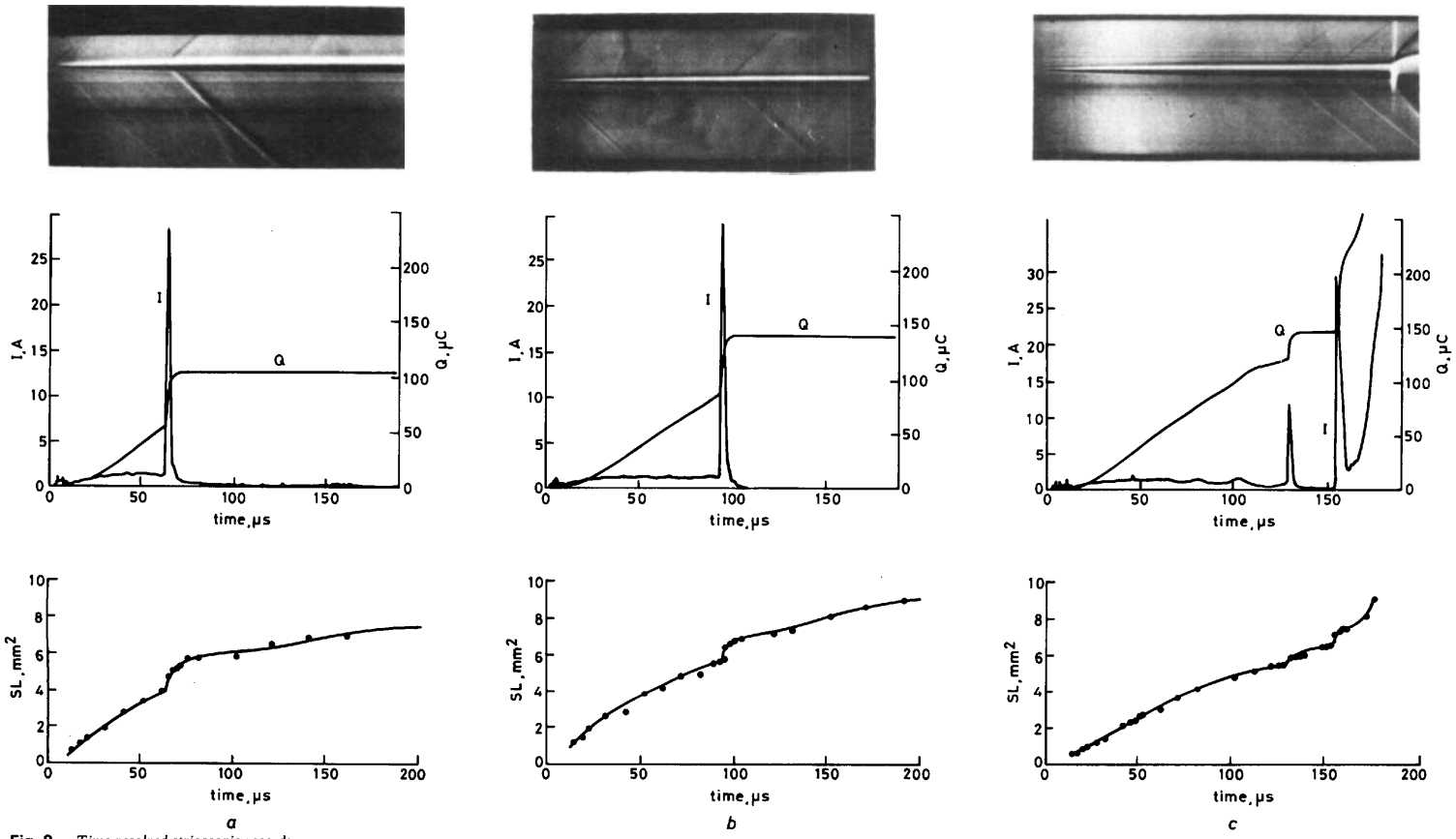

Fig. 8 *Time-resolved strioscopic records*

(*a*) $\Delta t = 60$ μs; (*b*) 90 μs; (*c*) 150 μs
Row 1: Strioscopic photographs Row 2: Current *I*; charge *Q* Row 3: Cross-sectional area *SL*

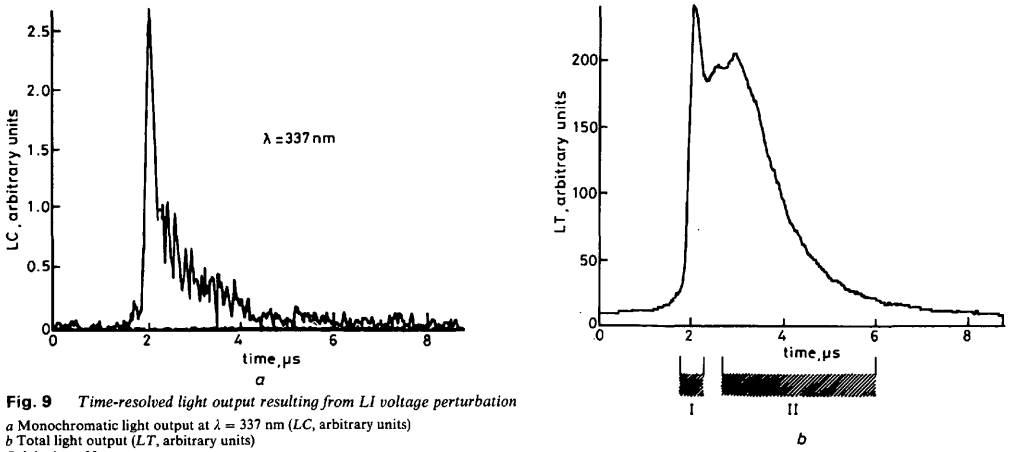

Fig. 9 *Time-resolved light output resulting from LI voltage perturbation*

a Monochromatic light output at $\lambda = 337$ nm (*LC*, arbitrary units)
b Total light output (*LT*, arbitrary units)
Origin $\Delta t = 90$ μs

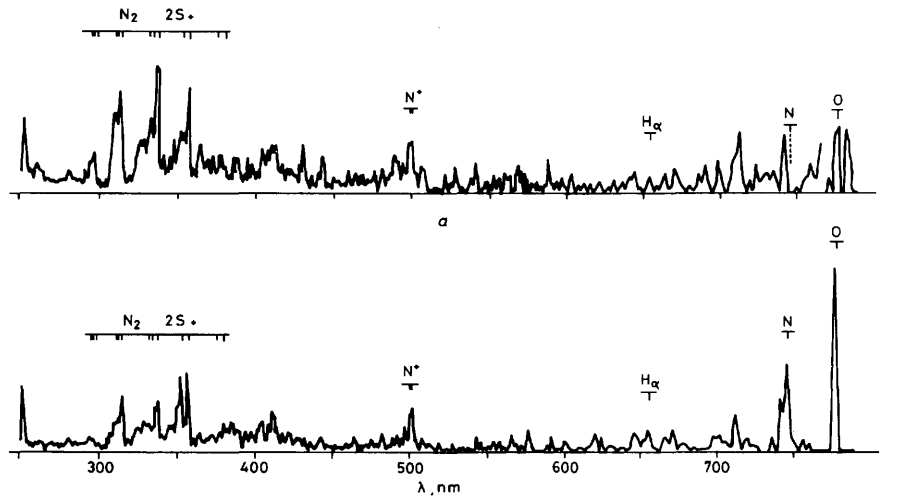

Fig. 10 *Discharge spectra at LI perturbation*

a Regime I: initial light peak *b* Regime II: subsequent emission

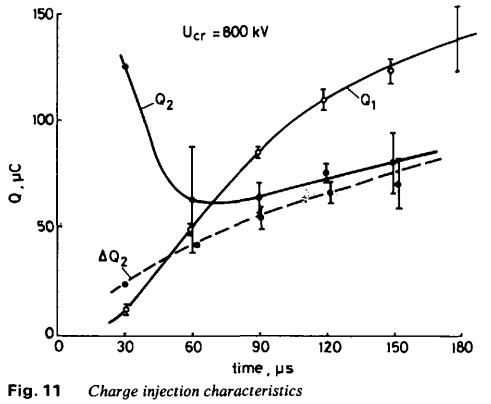

Fig. 11 *Charge injection characteristics*

step ΔQ_2 is more than 50% of the charge Q_1 previously injected. These data are for a negative voltage perturbation of -800 kV. Additional results for -1100 kV and for $\Delta t = 90$ μs did not show a significant increase of ΔQ_2. The upper curve shows the average value of the total charge injected after the voltage perturbation including ΔQ_2. In the case of breakdowns, they represent the charge flow up to the onset of the final jump. For withstand, it is a measure of the final charge value less Q_1. The large decrease in the value of Q_2 from the unperturbed region $\Delta t = 30$ μs to the choking region $\Delta t = 90$ μs is the result of the effect of ΔQ_2, in the leader corona, on the leader propagation. For longer Δt, Q_2 is little greater than ΔQ_2. This is because after the perturbation the discharge is either effectively stopped or proceeds rapidly to the final jump.

The step injection of charge ΔQ_2 arising from the voltage perturbation causes a corresponding increase of the space-charge fields at the plane. Fig. 12 represents the

average value of this step increase in the field ΔX_- at two locations on the plane, the axial probe L and the off-axis probe H at a radial distance of 1 m, as a function of Δt.

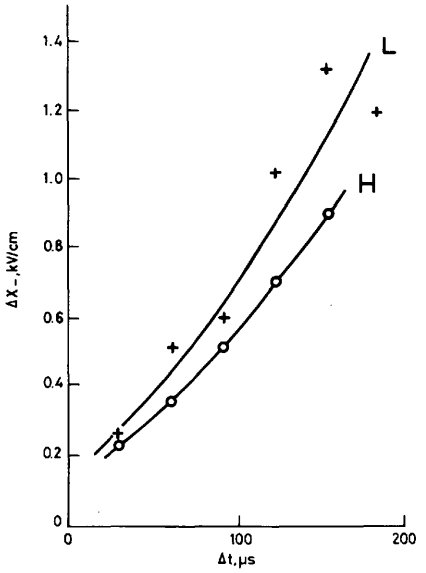

Fig. 12 *Space-charge field change caused by LI voltage perturbation at probes L and H for $U_- = 800$ kV*

The greater magnitude of ΔXL_- with respect to ΔXH_- is a consequence of the symmetrising effect of the averaging process, so that the Figure typifies an axial discharge growth. The field changes ΔX_- are approximately linear with Δt. Thus the saturating characteristic of ΔQ_2 with Δt is compensated by the closer approach with Δt of the leader-corona space charge to the plane.

The space-charge field change ΔXL_- arising from the perturbation is shown in Fig. 13 as a function of both the space-charge field ΔXL_+ (existing immediately prior to the perturbation) and the associated charge step ΔQ_2 following the perturbation. Fig. 13*a* shows that the ratio $\Delta XL_-/\Delta XL_+$ is about unity, i.e. the space charge field is approximately doubled by the perturbation. This occurs despite ΔQ_2 being little more than one half of Q_1, because the space charge causing ΔQ_2 is largely associated with the leader corona. The values of ΔXL_- and ΔQ_2 for individual discharges are given in Fig. 13*b*.

The total charge flow $Q(t)$ is accompanied by changes in the leader cross-section, as already noted in the strioscopic photographs. This relationship between the leader cross-sectional area $S(t)$ and the charge $Q(t)$ is shown in Fig. 14. In the perturbation region (broken curve) the charge input increases much more rapidly with respect to $S(t)$ than in the equilibrium regions on either side. This large power input causes an overpressure within the channel and shock-wave generation as observed in the photographs. It can also be seen in Fig. 14, that, in the case of withstand, the channel cross-section continues to increase after the cessation of charge flow; this is a manifestation of the relaxation processes and thermal diffusion which exist within the leader channel.

2.7 Discharge extension

Fig. 15*a* shows the nature of the spatial extension of the leader and leader-corona system when the voltage perturbation is applied. This sketch illustrates the continuous growth of the positive leader to an axial length Z_1, with associated corona length S_1, at the time of perturbation.

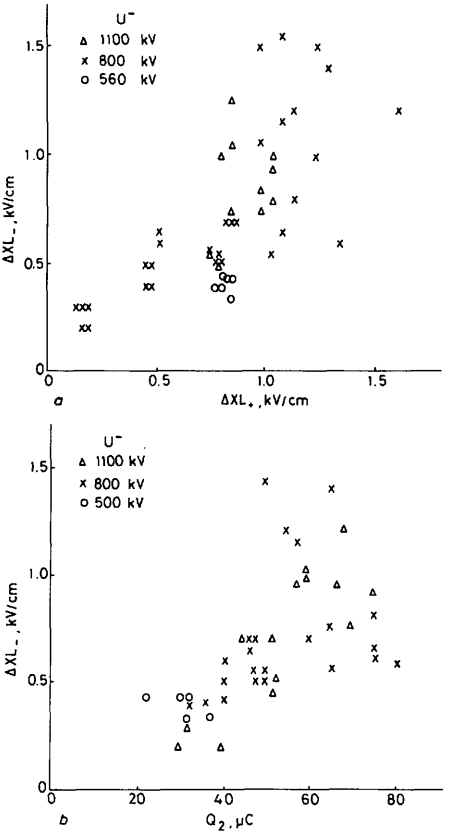

Fig. 13 *Space-charge field change ΔXL_- by LI voltage perturbation*
a ΔXL_-: dependence on ΔXL_+
b ΔXL_-: dependence on ΔQ_2

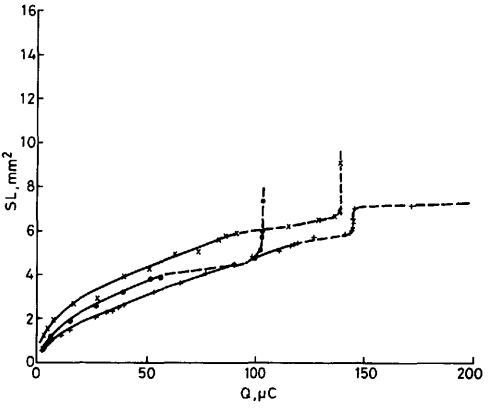

Fig. 14 *Correlation of leader cross-sectional area $S(t)$ and charge flow $Q(t)$*

Following the perturbation at Δt, the leader and its leader corona are suddenly extended to lengths Z_2 and S_2,

respectively. The leader growth may then continue either to a final length of Z_3 at time t_3 for the case of withstand, or may continue to the final-jump phase.

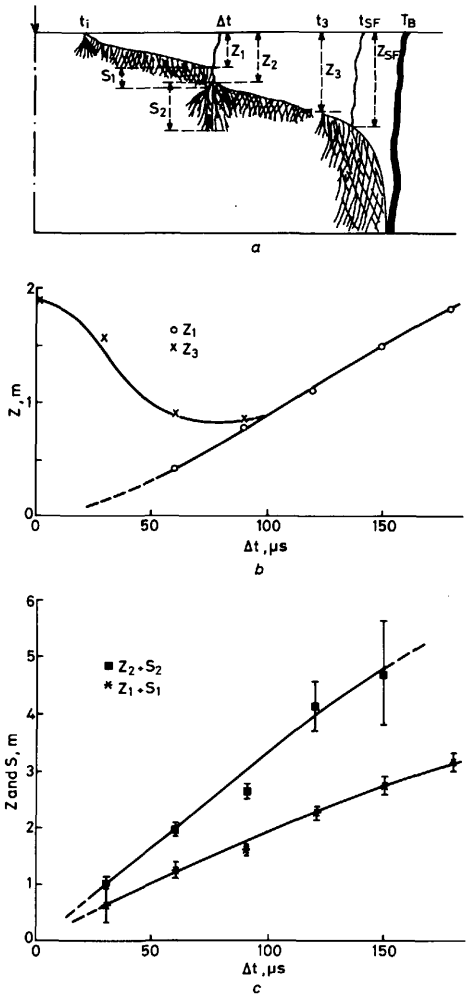

Fig. 15 *Effect of LI voltage perturbation on discharge leader and leader corona spatial extension*

a Definitions
b Axial leader lengths at Δt and t_3
c Overall discharge lengths immediately before and after the perturbation at Δt

The brightness of the discharge perturbation process prevented reliable measurement of Z_2 for a sufficient statistical study. However, Fig. 15*b* gives data for Z_1 and Z_3. For $\Delta t = 0$, Z_3 is the average axial leader length at withstand. The increase of Z_1 with Δt is a measure of normal positive leader growth at an axial velocity of about 1 cm/μs (compared with the average real velocity of about 1.5 cm/μs). The limiting length Z_3 exhibits a strong minimum because of the choking effect discussed earlier. Although Z_2 cannot be reliably measured, the total discharge length $Z_2 + S_2$ following perturbation is more easily found. Fig. 15*c* shows both $Z_1 + S_1$ and $Z_2 + S_2$, from which the overall discharge extension of up to 2 m caused by the perturbation is seen.

The probability of breakdown can be shown to depend on the value of Z_1 at the instant of voltage perturbation. Despite the small sample, this is clear from Fig. 16,

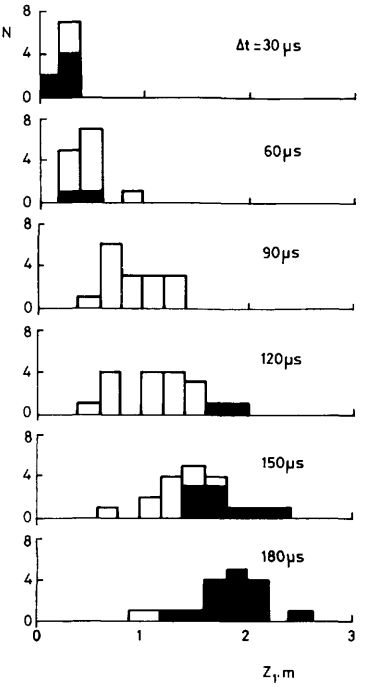

Fig. 16 *Histogram of leader length at time of LI voltage perturbation*
Breakdown events shaded

where histograms of Z_1 are shown for the case of $U^- = -800$ kV, and Δt varying from 30 μs to 180 μs. The leaders which resulted in breakdown of the gap are shaded. This illustrates all three régimes of behaviour; for $\Delta t = 30$ μs the breakdown probability is approximately 50%, and the cases of breakdown occur uniformly for all Z_1. At $\Delta t = 90$ μs, the choking effect prevents breakdown for all Z_1. For longer Δt, the breakdown probability increases for large Z_1, whereas leaders of shorter Z_1 may still be choked.

Fig. 17 quantifies the discharge extension associated with individual discharges. Fig. 17*a* shows $Z_2 + S_2$ as a function of Z_1, with Δt as a parameter. For $\Delta t = 90$ μs the effect of U^- on this relationship is given in Fig. 17*b*, from which it may be seen that the voltage increment which is necessary to cause a one metre extension of the discharge is approximately 400 kV. This value of 4 kV/cm is close to the generally accepted gradient associated with positive streamers.

The discharge current measurements and the leader-track analysis have been combined to give the relationships of Fig. 18. This shows five curves for voltage perturbations of different Δt values. The relationship between the instantaneous charge value $Q(t)$ and the real leader length $L(t)$ remains almost unchanged for all these cases. The current and velocity increases observed in the leader growth as a result of perturbation are thus linearly interrelated, and the nature of the channel appears unchanged as far as the charge flow per unit length is concerned. It should be noted that, because two leader channels were often present, the value of $L(t)$ in Fig. 18

represents the sum of the two leader lengths; thus the slope of about 50 μC/m is the actual charge per unit length on each channel.

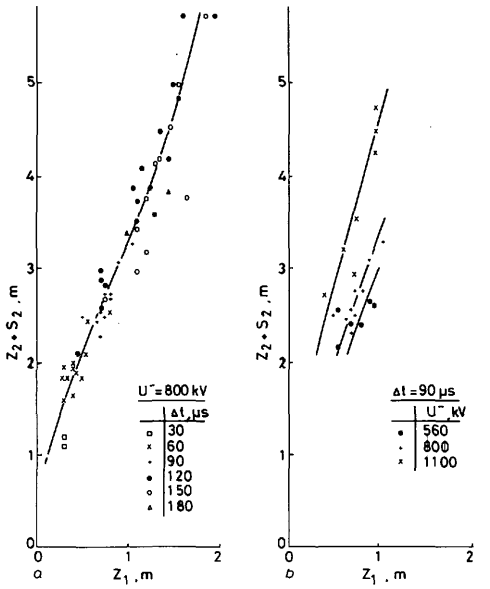

Fig. 17 *Discharge extension: influence of Δt and U_-*

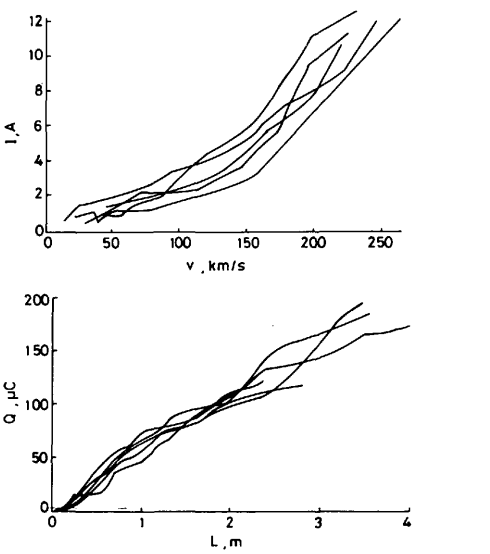

Fig. 18 *LI perturbations: correlation between electrical and spatial measurements*

Δt = 30–150 μs
Charge Q; real leader length L; current I; real leader velocity v

3 SI perturbations

3.1 Introduction

It has been seen that sudden perturbations of the LI type on the voltage front caused rapid electrical and spatial changes. Perturbations of the SI type may be expected to cause less discontinuous behaviour, but to have effects related to an increased slope of the voltage front and to an overvoltage of the gap.

The positive impulse was constant at 1455 kV (240/9000 μs) which corresponded to the U_{50}-σ level (σ = 75 kV). The negative switching impulse perturbation (100/1500 μs) had a crest value between −470 kV and −1200 kV. Two delay times, 60 μs and 120 μs, were used. The breakdown probability was 100% for all $U_- > -500$ kV.

3.2 Time-lag data

Fig. 19 shows the time to breakdown $\bar{T}_B$ as a function of U_- for both Δt values. For a perturbation of −470 kV, $\bar{T}_B$

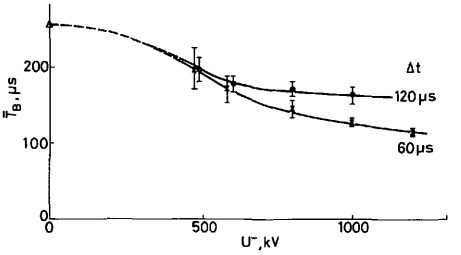

Fig. 19 *Time to breakdown dependence on SI perturbation amplitude U^- and delay Δt*

is reduced below the basic positive impulse value, but is not significantly dependent on Δt. For larger perturbations, $\bar{T}_B$ is significantly shorter at Δt = 60 μs, even though the total prospective crest potential difference is nearly the same. The acceleration of the discharge process by the change of slope of the voltage front is thus more effective at this earlier stage.

3.3 Transient response of discharge to SI perturbation

As suggested by the $\bar{T}_B$ data, the response of the discharge to this perturbation can be strongly dependent on Δt. Fig. 20 gives for both Δt values an example of image-convertor streak photographs, charge, current and positive and negative applied voltages. At Δt = 60 μs, the voltage perturbation occurs at a fairly early stage of leader growth. The leader channel is not significantly reilluminated, and the leader corona is little changed. Nevertheless, a small current spike accompanies the perturbation, and the leader current and velocity are somewhat larger than before the perturbation. This acceleration of the leader at an early stage is the cause of the strong reduction of $\bar{T}_B$. At Δt = 120 μs, the perturbation is superimposed on a much more fully developed leader. Some reillumination of the leader and a stronger change in the leader corona is found. The current spike following Δt is also larger here. The subsequent leader current, which had begun to decrease before Δt, is now 2 to 4 times greater and the leader velocity is increased. The final-jump phase follows within 20 to 50 μs; the total $\bar{T}_B$, however, is as long as with Δt = 60 μs despite the higher perturbation U^- in this example.

Fig. 21 shows the electric field changes at the central field probe L for the same two discharges as in Fig. 20. The total, geometric and space-charge fields, EL, GL and XL are displayed, together with the field/charge ratio XL/Q. The field changes occurring at Δt = 120 μs are greater, and the change of slope of the XL transient is very marked. The increase in value of the XL/Q ratio after Δt reflects the closer approach of the space charges to the plane as a result of perturbation.

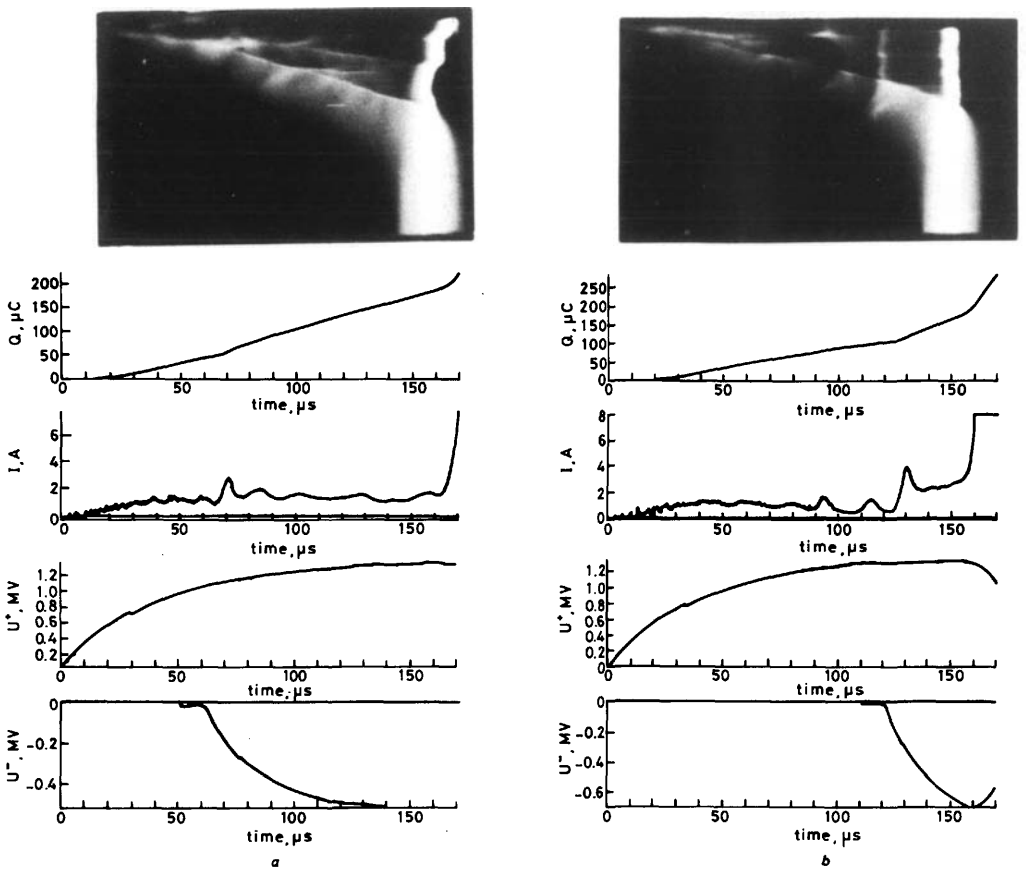

Fig. 20 *Test records of SI voltage perturbation*
(*a*) $\Delta t = 60$ μs; (*b*) $\Delta t = 120$ μs
Row 1: Image convertor photographs Row 2: Charge Q Row 3: Current I Row 4: Positive voltage U^+ Row 5: Negative perturbation voltage U^-

3.4 Leader track analysis

Detailed examination by digital reconstruction was again carried out in these experiments, as described for the LI perturbation tests in Section 2.3, Fig. 7. This confirms that the SI perturbation does not fundamentally change the charge/real-length and current/real-velocity relationships of the leader (Fig. 22). The scatter in the Q/L plots (slope 50 μC/m) are the result of nonvisible second leaders for breakdown events. This does not affect the I/v characteristic.

The acceleration of the leader real velocity following the perturbation was measured from high time-resolution image-convertor photographs. This velocity is shown in Fig. 23 to be an approximately linear function of the rate of change of the voltage difference $(U^+ + U^-)$ across the gap. The two velocity populations v_1 and v_2, existing immediately before and immediately after the perturbations, are commonly related to the change of voltage slope at Δt. The two velocities v_1 and v_2 are not, however, correlated with each other.

3.5 Temporal characteristics

The average variation of the charge behaviour with time, for the different values of the crest of the SI perturbation, is shown in Fig. 24 for both Δt. The perturbation in charge is consistent with the sample records given earlier. The similarity between these curves and the voltage-difference shapes again may be taken to reflect the dependence of leader propagation and current on the derivative of the voltage.

The average value of the leader length as a function of time is given in Fig. 25. The extension of the leader shows the effect of the crest value of the SI perturbation, but this is less marked than the effect on charge flow.

The space-charge field at the plane electrode shows large changes, indicating a greater influence of the charge flow than the leader extension. The data in Fig. 26 shows the temporal variation before and after the SI perturbation of $\bar{X}(t)$, which is the average value of the mean space-charge field measured at the three field probes L, K and H.

3.6 Partial chopping

In nonstandard surge shapes, regions of negative voltage slope dU/dt frequently occur. It is therefore useful to observe leader behaviour for reductions in the applied voltage. A brief study of these effects was included in these tests. The basic impulse shape to the rod electrode (240/9000 μs) was of a crest between 1668–2162 kV ($U_{50} + \sigma$ to $U_{50} + 6\sigma$). The partial chopping was effected by the application to the plane electrode of a +490 kV (100/1500 μs)

impulse at a Δt of 60 μs or 120 μs. No breakdowns were found even at $U_{50} + 6\sigma$. Fig. 27 gives image convertor and

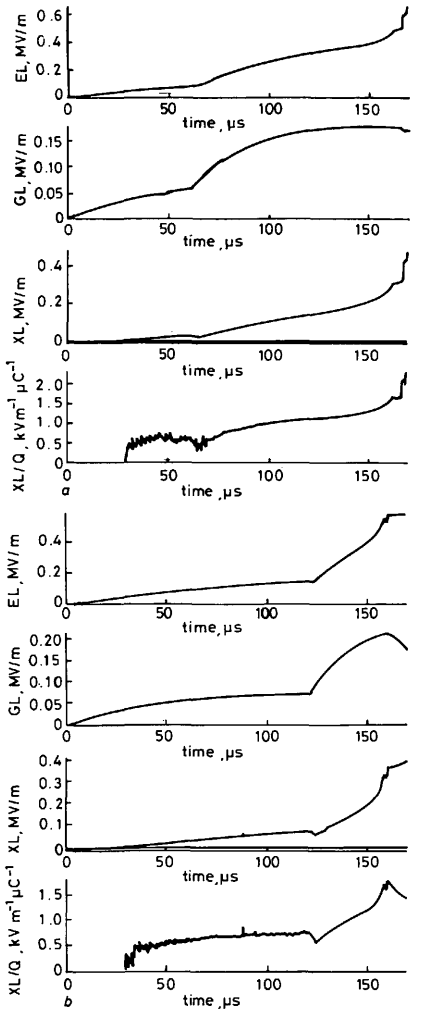

Fig. 21 *Electric field behaviour for SI voltage perturbation*
(*a*) Δt = 60 μs; (*b*) Δt = 120 μs
Row 1: Field, measured at probe, *L*, *EL*
Row 2: Geometric field *GL*
Row 3: Space-charge field *XL*
Row 4: Field/charge ratio *XL/Q*

electrical transient records for partial chopping at the two Δt values. For $\Delta t = 60$ μs, a significant further leader growth can occur, and the current flow is sometimes found to continue for up to 100 μs.

However it is at a reduced level, and contains peaks associated with weak reilluminations in the leader. The increase of charge and space-charge field is also slowed down. At $\Delta t = 120$ μs the partial chopping is especially effective in arresting leader development. A complete stoppage of growth occurs, even for $U^+ = 2162$ kV. No leader reilluminations or further charge or field increases occur.

The average charge flow characteristics are given in Fig. 28. The continuing charge flow after $\Delta t = 60$ μs at $U_+ = 1668$ kV is quantitatively shown here to amount to a further 50% after partial chopping. For $\Delta t = 120$ μs, no further charge flow occurred.

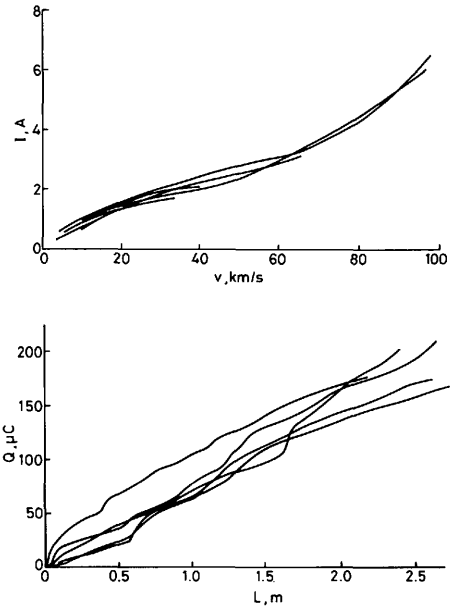

Fig. 22 *Leader track analysis for SI perturbation*
Δt = 60 μs and 120 μs
Current *I*; real leader velocity *v*; charge *Q*; real leader length *L*

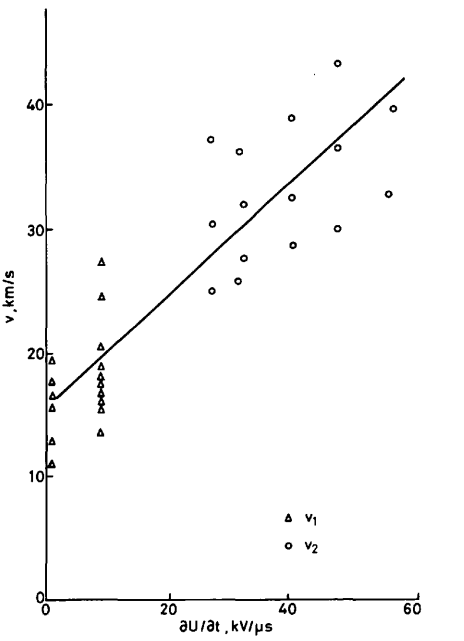

Fig. 23 *Leader velocity before and after SI perturbation correlation with rate of change of voltage*
v_1 = real leader velocity just before Δt
v_2 = real leader velocity just after Δt

4 Conclusion

Voltage perturbations of LI and SI shapes have been found to affect the discharge development in different ways, as the leader and leader-corona phases of the discharge were both influenced by the slope of the applied voltage.

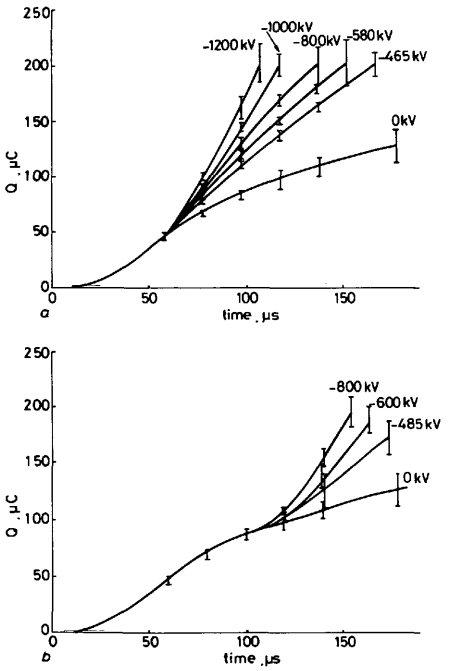

Fig. 24 *Temporal characteristics of charge: average values*
a $\Delta t = 60$ μs; *b* $\Delta t = 120$ μs
Labels indicate crest voltage of SI perturbation

For perturbations applied to a basic positive impulse of the critical time to crest, which was the case in these tests, the time of application Δt of the perturbation voltage on the basic impulse front was also an important parameter.

4.1 LI perturbations

(*a*) If the voltage perturbation was applied at an early stage of leader development, namely up to an axial length of about 0.5 m in the 6 m gap, the probability of breakdown was almost unchanged. On this basis, this can be defined as the unperturbed region, although minor transient changes could be seen in the discharge structure. This region corresponds to a perturbation delay Δt of up to about 60 μs.

(*b*) When the LI perturbation was applied at a time around 90 μs, at which time the average axial leader length was 1 m or more, the discharge was arrested so effectively that even a 30% increase in the perturbation voltage failed to cause breakdown. The cause of this choking effect was a large transient ionisation growth in the leader and leader-corona system. In the leader itself, the equilibrium condition supporting stable propagation is disturbed. For the leader corona, a strong retarding space-charge field is created, and the large corona extension into low-field regions is itself unstable following the perturbation.

(*c*) In the choking region, the space-charge flow caused a large increase in the space-charge field at the plane, and

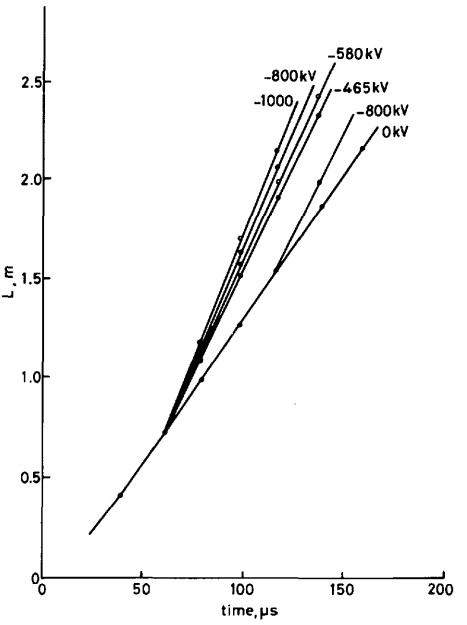

Fig. 25 *Temporal characteristics of leader real length: average values*
Labels indicate crest voltage of SI perturbation

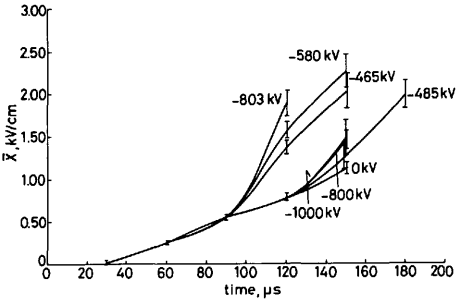

Fig. 26 *Temporal characteristics of space-charge field in central region of plane: average values*
Labels indicate crest voltage of SI perturbation

the streamers of the leader corona were sometimes observed to traverse the gap. This interaction with the plane would normally have initiated the final-jump phase, and breakdown would have been inevitable. But the effects causing discharge arrest remain dominant.

(*d*) The image-convertor, current and photomultiplier measurements showed that the leader and corona system perturbation occurred in two stages. A fast transient illumination of the leader, with little charge flow, was an indication of the voltage front propagation which is necessary to increase the leader tip potential. The large corona which then followed this potential increase was responsible for the charge injection by the perturbation.

(*e*) A quantitative comparison of the discharge extension with the voltage perturbation indicates that the increased voltage gradient in the gap may be concentrated mainly as

an electric field of about 4 kV/cm within the extended leader-corona streamers.

observed in these tests, and the time to breakdown $\bar{T}_B$ was decreased.

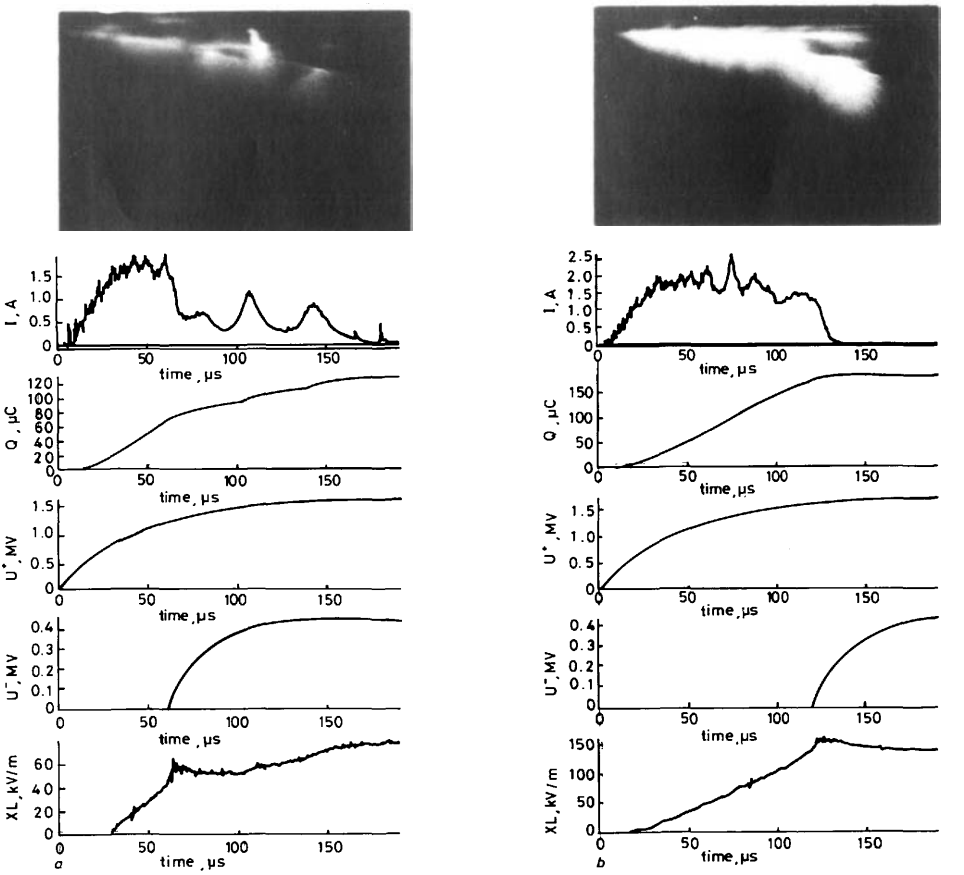

Fig. 27 *Test records of partial chopping by SI voltage perturbation*

(*a*) $\Delta t = 60$ μs; (*b*) $\Delta t = 120$ μs
Row 1: Image convertor photographs
Row 2: Current I
Row 3: Charge Q
Row 4: Positive voltage U^+
Row 5: Negative voltage U^-
Row 6: Space-charge field XL

(*f*) The application of the perturbation causes an overpressure to be developed within the channel. This results in a shock wave from the boundary of the leader channel at the instant Δt. The cause of this overpressure is the large current increase, accompanied by a rapid elevation of temperature. Additional evidence is provided by the spectroscopic observations: a large increase in number density is caused by molecular dissociation within the leader as well as the temperature rise. This overpressure relaxes rapidly to a subsonic expansion.

(*g*) A 3-dimensional analysis of the leader growth has enabled the response of the real leader velocity to be measured. This enables the important charge per metre characteristic of the leader to be found. This appears to remain approximately constant at the value of 50 μC/m, which is typical of normal positive leader growth. This constancy is important for modelling of the perturbed discharge.

4.2 SI perturbations

(*a*) Because of the long-duration overvoltage caused by an additive SI perturbation, breakdown was nearly always

(*b*) The earlier the time Δt of application of the perturbation, the greater the reduction of $\bar{T}_B$, because of the earlier acceleration of the leader.

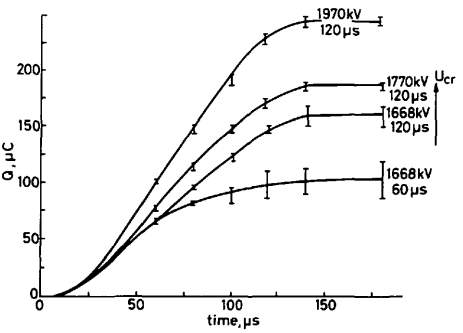

Fig. 28 *Partial chopping: temporal characteristics of charge flow: average values*

Labels indicate crest voltage of basic positive impulse and time Δt of partial chopping

(*c*) The effects observed on the discharge growth depended not only on the time of the perturbation, but also on the change of voltage slope caused by its application.

(*d*) Time-resolved photographs showed little change in leader-corona structure for SI perturbations.

(*e*) Real leader length measurements again showed that the charge per metre characteristic value of 50 μC/m was unchanged.

(*f*) The increase observed to occur in leader current and real velocity were shown, following a transient condition at Δt, to be proportional to the voltage derivative dU/dt of the total gap voltage (basic impulse and perturbation). This property may again form a useful parameter for modelling of nonstandard impulse breakdown.

(*g*) The effect of a reduction of dU/dt by partial chopping with an opposing SI perturbation has been shown to depend on Δt. The arrest of the discharge is more effective for longer Δt and thus longer leader lengths. In this case, withstands resulted even for large overvoltages, because of the difficulty of re-establishing stable propagation conditions with the leader-streamer system after this type of perturbation.

5 References

1 GALLIMBERTI, I., BADALONI, S., HARTMANN, G., and KLEWE, R.C.: 'Time resolved spectroscopic measurements of the discharge phenomena', *Electra.*, 1972, (23), pp. 137–147

2 GALLIMBERTI, I., HARTMANN, G., and MARODE, E.: 'The leader to spark transition', *ibid.*, 1975, (53), pp. 123–132

3 BORDAGE, M.C., and HARTMANN, G.: 'Spectroscopic measurements on discharges along a dielectric surface', *J. Appl. Phys.*, 1982, **53**, pp. 8568–8576

4 GALLIMBERTI, I., HEPWORTH, J.K., and KLEWE, R.C.: 'Spectroscopic investigation of impulse corona discharges', *J. Phys. D.: Appl. Phys.*, 1974, **7**, pp. 880–898

5 HARTMANN, G.: *C.R. Acad. Sci.*, 1972, **274(B)**, p. 703

6 HARTMANN, G.: 'Etude par spectroscopie des mecanismes des collisions dans la partie active ionisante de la charge d'espace d'une decharge couronne'. Ph.D.Thesis, 1977, Orsay

7 LOCHTE-HOLTGREVEN, W.: 'Plasma diagnostics' (North-Holland Publishing Company, Amsterdam, 1968)

8 GRIEM, H.R.: 'Plasma spectroscopy' (McGraw Hill, New York, 1964)

9 Les Renardières Group: 'Positive discharges in long air gaps at Les Renardières — 1975 results and conclusions', *Electra*, 1977, (53), pp. 31–153

10 Les Renardières Group: 'Negative discharges in long air gaps at Les Renardières — results', *ibid.*, 1981, (74), pp. 193–201

11 RÜHLING, F.: 'Calibration method for quantitative analysis of discharge channel diameter'. 51-08, ISH Milan, 1979

12 GIBERT, A. *et al.*: 'Schlieren techniques and long air gap discharges'. Int. Conf. Atmospheric Electricity, Albany, NY, USA, 1984

13*a* BAYLE, P., BAYLE, M., and FORN, G.: 'Neutral heating in glow to spark transition in air and nitrogen', *J. Phys. D*, 1985, **18**, (12), pp. 2395–2416

13*b* BAYLE, P., BAYLE, M., and FORN, G.: 'Blast wave propagation in glow to spark transition in air', *ibid.*, 1985, **18**, (12), pp. 2417–2432

14 HIDAKA, K., and MUROOKA, Y.: 'Electric field measurements in long gap discharge using Pockels device', *IEE Proc. A*, 1985, **132**, (3), pp. 139–146

15 LEROY, G., GARY, C., HUTZLER, B., LALOT, J., and DUBANTON, C.: 'Les propriétés diélectriques de l'air et les très hautes tensions'. Editions (Eyrolles, 1984)

16 Les Renardières Group: 'Long air discharges at Les Renardières — 1973 results', *Electra*, 1974, (35), pp. 49–156

17 GALLIMBERTI, I.: 'The mechanism of the long spark formation', *J. Phys. Lett.*, 1979, Colloque C7, suppl. 7, (40), pp. 193–250

18 GALLIMBERT, I., GOLDIN, M., and POLI, E.: 'Electric field calculation in long gap discharges', *4th Int. Symp. H. V. Eng.*, Athens, 1983

19 GALLIMBERTI, I., GOLDIN, M., and POLI, E.: 'Field calculations for modelling long sparks'. Padova University Report UPee 82/07, 1982

20 GALLIMBERTI, I.: 'A thermodynamic model of the leader channel', *Electra*, 1977, (53), pp. 89–97

21 GALLIMBERTI, I., GOLDIN, M., and POLI, E.: 'A computer model of leader-streamer propagation in long sparks'. *4th Int. Symp. H. V. Eng.*, 1983, Athens

22 GALLIMBERTI, I.: 'A computer model for streamer propagation', *J. Phys. D: Appl. Phys.*, 1972, **5**, pp. 2179–2189

23 GALLIMBERTI, I.: 'Mathematical models for the streamer formation in non-uniform gaps'. Padua University, Report UPee 72/04, 1972

6 Appendixes

6.1 Spectroscopic analysis of the leader reillumination

S. BADALONI, I. GALLIMBERTI, AND G. HARTMANN

6.1.1 Introduction: Spectroscopic measurements are often used in gas discharge studies as a diagnostic technique to obtain information on the internal conditions of the plasma channels: from the relative intensities of different bands and lines the temperature of electrons and gas molecules can be estimated.

In previous experiments of the Les Renardières Group, spectroscopic results of the different discharge phases, under positive switching surges, have been collected. In 1972 the spectrum of the leader corona and of the leader channel were obtained in the range 220–780 nm, by using two monochromators scanning the spectrum during a long sequence of shots [1]. However, while the leader corona spectrum was obtained with good sensitivity and reliability, the leader channel spectrum was not equally satisfactory, due to the weak emission. Quantitative measurements were possible only during the channel restrikes, which appeared at random times with random intensities.

In 1975, the leader channel spectrum was obtained with a spectrograph and time-resolved with an image convertor camera [2]. Again, owing to the relatively weak emission, the spectra were reliable only during the final jump and the transition to the arc. For the present test period, the spectroscopic measuring apparatus (one monochromator with two photomultipliers for total and monochromatic lights; see Section 2, Part 1) was specially designed for the best reliability of the results. It has been applied to study the leader emission during reilluminations caused by the voltage perturbations ($\Delta t = 90$ μs), to obtain the maximum light intensity and the minimum scatter from shot to shot.

In Section 2.5 some of the spectroscopic results obtained have been presented. The most intense lines and bands that have been observed belong to the molecular and atomic systems of nitrogen and oxygen; also lines of ionised atomic hydrogen are present. It has also been seen that the spectrum is changing with time, and two time windows have been defined for light integration and quantitative comparison (Fig. 9). They correspond essentially to the propagation of a potential wave and to the injection of the corona current into the leader channel.

In this paper some more details are reported on the time sequence of the observed phenomena; then a more analytic identification of bands and lines is proposed and a comparative discussion of the actual and previous results is presented.

Some specific spectral components have been selected and their time evolution has been studied to obtain information on the leader internal conditions and their changes during the reillumination period.

6.1.2 Leader reillumination statistical scatter: As the time-resolved spectrum was obtained by scanning the whole wavelength range in a series of about 600 consecutive shots, its reliability depends on signal synchronisation and discharge reproducibility. All statistical effects related to the experiments' execution have therefore been carefully

analysed. The delay Δt_r between the trigger pulse that fires the negative voltage generator and the recording digitisers, and the steep front of the total light signal has been systematically measured. Fig. 29 reports the relative positions

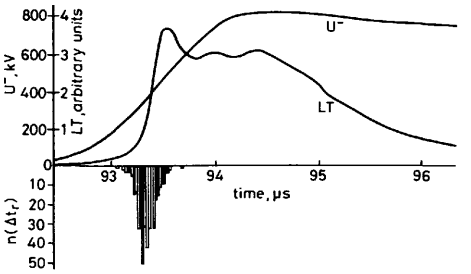

Fig. 29 *Statistics of leader reillumination inception: perturbation voltage U_-, total light intensity LT, and histogram of inception time lags*

of the average voltage perturbation and the average total light pulse, together with the statistical distribution of Δt_r. This distribution is very narrow (standard deviation $\sigma_{\Delta t_r} = 80$ ns) its scatter range $2\sigma_{\Delta t_r}$ compares very well with the measured jitter in the firing of the voltage generator (170 ns). It can therefore be assumed that the statistical fluctuations in Δt_r are better associated with the start of the voltage perturbation than with the inception of the reillumination processes. The latter occurs at a reproducible level on the voltage front; and the signal synchronisation errors are negligible.

The measured charge Q_1 that has flowed into the leader channel up to the time of reillumination inception ($t_r = \Delta t + \Delta t_r$) presents a coefficient of variation smaller than 3%, which indicates that the conditions within the leader channel just before the reillumination are highly reproducible. Also the peak current I_2 and the total charge ΔQ_2 during the reillumination have a small scatter (less than 8%), which ensures that the reillumination characteristics do not vary significantly from shot to shot. The obtained time-resolved spectra can be therefore assumed to be reliable and not affected by random fluctuations or jitter in signal synchronisation.

6.1.3 Identification of the spectral components: Each of the signals of monochromatic or total light has been processed automatically by computer: first the random noise has been digitally filtered, and the systematic noise, due to generator firing, measured by averaging the 'dark signal', has been subtracted; then the monochromatic intensity has been normalised on the total light signal; and finally the relative intensity has been integrated over the two selected time windows (see Fig. 9). The two spectra obtained with this procedure are reported in Fig. 30 (i and ii); for comparison the spectra of a leader discharge gliding on an insulating surface [3] are reported (*a* and *b*). In the first row (*a*) the spectrum of the surface leader head (corona to leader transition) is presented. It is essentially composed of the molecular emission of nitrogen: the second positive system ($2s+$), and a weak emission of the first positive system ($1s+$) together with some bands of the high-energy singlet state transitions and of the N_2^+ first negative system. It appears very similar to the streamer spectra measured in atmospheric air in both short and long gaps [4–6].

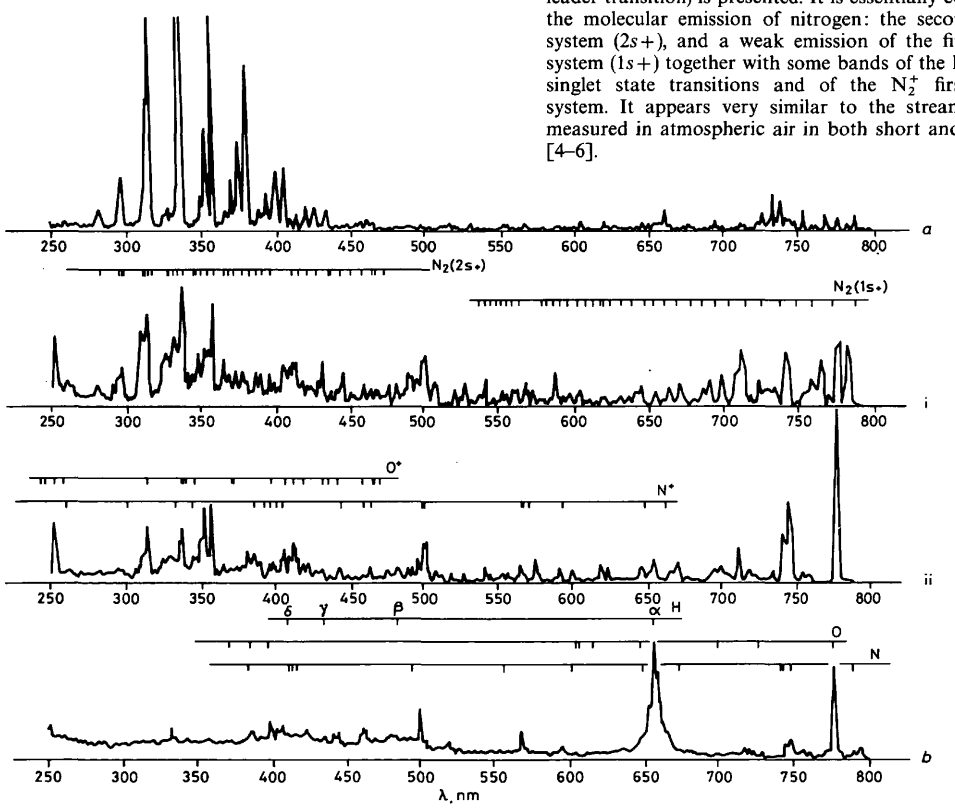

Fig. 30 *Spectra of leader reillumination*

(i) during the wave of potential gradient
(ii) during the leader corona charge injection
(*a*) spectrum emitted by the head of a surface gliding leader [3]
(*b*) spectrum emitted by the body of a surface gliding leader [3]

In the fourth row (*b*) the spectrum of the surface leader body is presented: it is composed of a continuum background with most of the more intense lines of the dissociated atoms of nitrogen, oxygen and hydrogen; also the ionised atoms N^+ and O^+ give some contribution to the spectrum.

These two spectra have been reported here because they represent the extreme cases of the leader channel plasma. In the transition region the gas is still in molecular form and the plasma is very far from local thermodynamic equilibrium (LTE), with a gas temperature T_g ranging from 300 K to 1500 K and an electron temperature T_e around 50 000 K. However, in the body of the channel the gas is fully dissociated and the plasma has reached LTE conditions, with $T_g \simeq T_e$ of the order of 20 000 K [3].

The spectra of the leader channel during the reilluminations present intermediate characteristics between these two extreme cases.

In phase (i), the N_2 second positive system can be clearly identified, with a relatively high intensity. The N_2 first positive system is also present with an intensity which is higher than in case (*a*). Some lines of dissociated oxygen can be observed while the atomic lines of nitrogen are practically absent, whereas some bright lines of ionised atoms N^+ and O^+ can be observed.

This indicates that in phase (i) the gas temperature is higher than in the head of the gliding leader: the O_2 molecules are partly dissociated, but the gas temperature is not high enough for dissociation of N_2, which needs a higher energy than O_2 (9.75 and 5.08 eV, respectively). The N_2 molecules are partly excited in the metastable $A^3\Sigma u^+$ state and in the long-life vibrational states, which favours the population of the $B^3\Pi g$ state and the emission of the first positive system; the electron temperature should be relatively high, but smaller than in the gliding leader head because the N_2^+ first negative bands and the transitions between the high energy N_2 singlet states are not observed.

In phase (ii) the N_2 second positive system appears much weaker than in phase (i); the N_2 first positive system has almost disappeared, while many atomic lines of oxygen, nitrogen and hydrogen appear with a relatively high intensity; the spectrum portion in the range 500–800 nm is very similar to that observed in the body of the gliding leader (except for the intensity of the H_α line, which comes from the dissociation of the plexiglass molecules in the case of the surface discharge). This indicates a rise in gas temperature with respect to phase (i), which causes an increase in N_2 and O_2 dissociation, and probably a decrease in electron temperature. Also a weak background continuum component can be identified in this phase.

6.1.4 Time evolution of the spectral components: Some of the brightest lines and bands of each spectral system have been selected to be representative of the whole system: the most intense bands of the second positive system have been added to give a representative signal for the N_2 molecular emission; the same has been done with a few atomic lines of N, O and H to represent the emission of the dissociated components. The most intense group of N^+ lines around 500 nm ($3d^3F \rightarrow 3p^3D$) has been used as representative of the emission of ionised atoms.

In Fig. 31 the time evolution of these components is reported, together with the voltage perturbation front and the current and total light pulses. The three spectral components have very different patterns: the ionised atom emission increases smoothly with the perturbation voltage; the molecular emission increases abruptly just before the current rise and it decays with a relatively fast time constant; the atomic emission is delayed with respect to the other two and reaches its maximum in correspondence

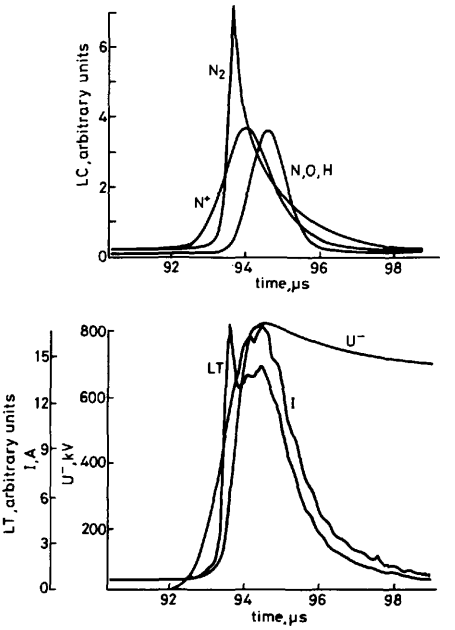

Fig. 31 *Time evolution of different spectral components: N_2 molecular emission; N^+ ion emission; N, O, H atomic emission*

The signals of applied voltage U_-, current I, and total light LT are also reported for comparison

with the current peak value. It is clear that the total light derives from the combination of the patterns of these spectral components.

When the voltage perturbation is applied, the voltage drop along the leader channel and the potential at its tip are raised. As a consequence, the current increases smoothly up to a time (93.5 μs in Fig. 31) at which a new large corona starts from the leader head. From this time, the current increases in a large bell-shaped pulse due to the corona charge injection into the channel head. During the present experiment, it has been shown (Appendix 6.4) that the electron density in the channel varies almost proportionally to the current. The inception of the leader corona (at $t = 93.5$ μs) produces a potential wave which travels along the leader and ionises the gas molecules. This corresponds to the phase (i) reported in Fig. 9: in this phase a sharp rise of the molecular N_2 emission appears due to both the propagating field front and the electron density increase.

The relatively fast decay time constant of the N_2 emission is probably associated with an increase of the dissociation processes within the leader channel, due to the increase of both temperature and electron density. This is consistent with the delayed appearance of the atomic emission which reaches the maximum intensity, together with the current, and then varies proportionally to the current itself.

The behaviour of the N^+ emission is more difficult to explain. The intensity rises just after the voltage application much earlier than the charge injection; then it does not appear to vary in proportion to the electron density. The upper level of the observed lines ($3d^3F$) lies 23.1 eV

above the ion ground state, so that its population would be very low under LTE conditions. The observed emission appears therefore anomalous for both intensity and time evolution. A tentative explanation of this behaviour will be given in the following.

6.1.5 Leader channel thermodynamic characteristics: A quantitative estimate of the characteristics of the leader channel plasma from the present results is very difficult: in fact the observed spectra indicate that LTE is not realised with the channel. Owing to the longitudinal electric field, the electrons have a higher temperature than the neutral molecules and transfer energy from the field to them in elastic and inelastic collision. However, in phase (i) some atomic lines of oxygen have been observed while the atomic lines of nitrogen are absent. This indicates a gas temperature T_g in the range 4000–5000 K, where the dissociated oxygen population largely exceeds that of dissociated nitrogen [2]. In phase (ii) the temperature T_g should increase because all the O, N and H atomic lines appear and the N_2 molecular emission decreases. A temperature range 5000–6000 K seems appropriate for this phase. These temperature ranges represent first approximation estimates because the gas is not in LTE conditions and dissociation is caused also by the electrons drifting in the electric field.

The electron temperature T_e can be estimated on the basis of the energy exchanges between electrons and neutral particles in the plasma. A stationary value of T_e state can be reached when the energy transfer from the electrons, because of the temperature difference $T_e - T_g$, is equal to the energy gain from the field [7]:

$$\frac{3}{2}k(T_e - T_g)f = e\mu_e E^2 \frac{\bar{\lambda}}{v} \tag{1}$$

where f represents the fractional energy loss per electron collision, μ_e the electron mobility, $\bar{\lambda}$ and v the electron mean free path and velocity, respectively. In this equation, it is implicitly assumed that the main process of electron energy relaxation is by elastic collision. This yields

$$\frac{T_e - T_g}{T_e} = \left[\frac{\bar{\lambda}eE}{\frac{3}{2}kT_e}\right]^2 \frac{1}{2f} \tag{2}$$

In Appendix 6.4 the values of the electric field in the leader channel have been derived as a function of the injected charge; they range from 5 to 0.5 kV/cm and can be plotted as a function of the gas temperature T_g (Fig. 32). On this basis, from eqn. 2 the electron temperature has been calculated. It does not vary much from a newly formed leader section ($T_g = 1000$ K) to an old leader section ($T_g = 6000$ K). The fields reported in Appendix 6.4 just before and just after the voltage perturbation are about 1.0 kV/cm and 0.85 kV/cm, respectively, and correspond to $T_g \simeq 5000$ and 6000 K and $T_e \simeq 15\,300$ and 14 700 K, respectively. These gas temperatures are in good agreement with the spectroscopic estimates.

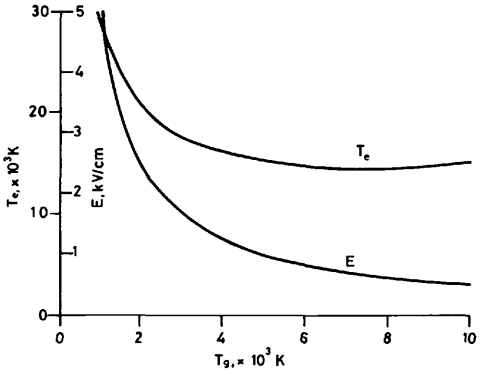

Fig. 32 *The field E and the electron temperature T_e in the leader channel as functions of the gas temperature T_g*

The convergent T_g and T_e characteristics in Fig. 32 indicate that the leader plasma tends to an LTE condition when it becomes older. The electron temperature values in Fig. 32 have to be considered upper limits, because the inelastic collisions accelerate the energy relaxation processes and lead to a lower T_e.

Let us now consider the emission of the N^+ lines. Just before the voltage perturbation, $T_e \simeq 3T_g$ and the population of each excited state depends on both temperatures. The equivalent temperature of the excited states (which defines its population through the Boltzmann factor) assumes an intermediate value between T_e and T_g, depending on the population and depopulation rates. The electron collisional population rates increase with the energy level of the state, because the impact cross-section increases [8]. Conversely, the quenching depopulation rates decrease with the energy level because of the energy and momentum transfer rules. As a consequence the low-level states assume equivalent temperatures not far from T_g, while the high-energy levels assume temperatures near T_e. The population of the different energy levels can therefore assume a quasistationary distribution, following a Boltzmann law with increasing temperature: each state is populated by electron collisions from the lower lying level at lower temperature. This can explain the high population of the N^+ $3d^3F$ state, which would be almost in equilibrium with T_e, and the high intensity of the emitted lines, as soon as the voltage perturbation is applied. However, at the moment of charge injection this intensity cannot increase proportionally to the electron density, because the lower levels from which the $3d^3F$ state is populated are pumped up and rapidly depleted because of their limited population. The emission is therefore saturated. On the contrary, the N_2 molecular bands are populated from the N_2 ground state, which cannot be depleted, and hence the emission intensity increases almost proportionally to the electron density, until it starts to decrease because of dissociation.

6.1.6 Conclusions: The specially designed measuring system and the careful synchronisation of the signals have made it possible to obtain time-resolved spectra of the leader channel during the reilluminations. The main spectral components are the molecular bands and atomic lines of nitrogen and oxygen, together with some lines of ionised atoms.

The time evolution of each spectral component has been derived and discussed to obtain information on the plasma internal conditions. Gas and electron temperatures have been estimated which are consistent with the leader characteristics deduced from electrical measurements.

6.2 On the leader diameter derived from density profiles of static pictures

F. RÜHLING

6.2.1 Introduction: One of the standard techniques used for the optical study of long sparks is static photography. If the photographic arrangement and the film properties

are adequately selected, the static picture not only permits spark track analysis, but also enables the leader diameter to be measured [9]. As this measurement yields the diameter of the final state of the channel, it is confined to the case of a voltage withstand.

6.2.2 Measurement of leader diameter: The leader diameter is measured from the microdensitometer plot of the density profile across the micro-image of the leader track. To obtain a measurable size of the image, a teleobjective is needed for long-spark experiments. The visible light emitted by the leader channel was recorded by a camera which had an ordinary glass 135 mm *f*4 teleobjective. With this photographic arrangement [9, 10], it proved to be convenient to use a 400 ASA film, with respect to grain size and density-exposure characteristic. If A and f denote the distance of the gap axis and the focal length of the objective, respectively, the demagnification of the image [11] becomes

$$R = A/f - 2 = 129 \tag{3}$$

in the present experiment.

The typical image density profile of a leader section is similar to the Gaussian error distribution curve. The width of this profile d_{ph} at half amplitude (Fig. 33*a*) is considered to be significant for the photographic leader diameter [9, 10].

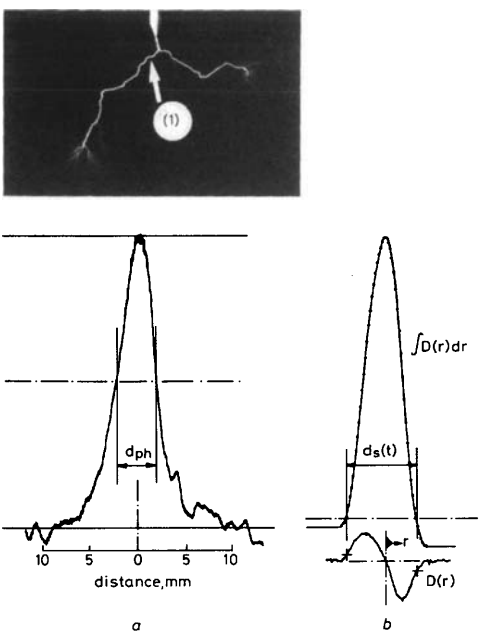

Fig. 33 *(a) Typical image density profile of a leader section measured at (1) and (b) modified profile obtained by integrating the image density curve D(r) of a schlieren record (see Fig. 38)*

a Definition of the photographic diameter d_{ph}
b Definition of the diameter $d_s(t)$ derived from $D(r)$

Fig. 33*b* refers to Fig. 8*a* and illustrates the relationship of this density profile to the image density output of a schlieren record using slit-streak technique. When that record is analysed by a microdensitometer (Appendix 6.3) the image density fluctuation across a leader section then produces a kind of radial image density $D(r)$, which is fairly similar in overall shape to the sine curve. The integral of this curve (Fig. 33*b*) is comparable to the image density profile derived from static pictures. Owing to the definition of the time-dependent diameter $d_s(t)$ of a schlieren record, the theoretical boundaries of the channel are defined much more off-axis than those derived from static pictures. It remains for further analysis to consider the correlation of the integral of $D(r)$ to leader channel properties. It is assumed that the integral approximately indicates the variation of neutral particle density, whereas $D(r)$ is a measure of changes in the refraction index according to variations in the density of the neutral species [12].

6.2.3 Comparison of static photography with schlieren technique: For impulse tests the relevant final diameter of the leader is that one which exists at the end of the leader propagation. At that time the impulse current has decreased to zero. The associated value d_0 can be measured from the slit-streak schlieren record.

As the leader channel continues to expand, the imprint of the leader on the film implies a larger diameter d_{ph} according to the definition of Fig. 33.

Measurements from both methods for the same shot are comparable. Owing to the tortuosity of the leader track, different values of d_{ph} can be measured. The bars in Fig. 34 indicate the scattering of d_{ph}. Using the approximation

$$d_0 = 1.7(d_{ph} - 2.5), \text{ mm}$$

the diameter d_0 at the end of leader activity can also be estimated from static pictures. This relation is obtained from the 'voltage perturbation' experiment (Section 2.4).

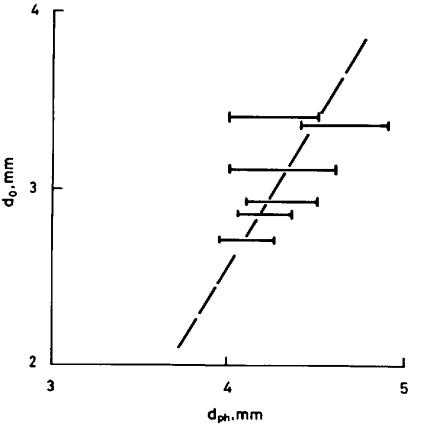

Fig. 34 *Correlation between the photographic diameter d_{ph} and the diameter d_0 derived from schlieren records at the time at which the leader current has decreased to zero (see Fig. 8)*

6.2.4 Features of the photographic leader image: During the application of the first impulse usually two leaders develop simultaneously (Section 2.5). Fig. 35*a* gives an example for a short basic leader, which is reactivated after $\Delta t = 400$ μs to nearly the same length as the nonreactivated one. The reactivation phase is associated with 50 μC of additional charge injection (Fig. 36*a*). It is clear from Fig. 35 that three different leader diameters can be measured. The reactivated leader (1) provides an extremely large image density profile, which is probably due to the channel expansion during the delay of Δt to the application of the negative voltage (Fig. 36*b*).

However, the old long leader is only partially affected by the reactivation of the short one. The first part (2)

differs clearly in the width of the channel from the second part (3), assuming that it is deionised after Δt. There is some evidence that the first part has kept a sufficiently high ionisation rate with respect to the conductivity return. This phenomenon can only be observed during long reactivation phases.

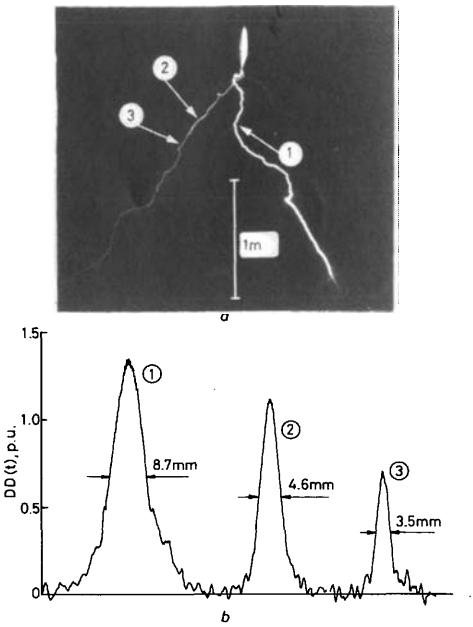

Fig. 35 *(a) Static picture during 'leader decay' experiment (combination 1(a), Δt = 400 μs) and (b) associated image density profiles of leader sections at points (1), (2), and (3)*

a { Right leader: short basic leader before reactivation
Left leader: long basic leader, non-reactivated }

It is evident from static photography that the positive leader which propagates into a space-charge field (Section 4) is much brighter than the standard leader. The image density profile of Fig. 37*b* gives an example. It represents a large leader diameter of 6.6 mm and has a peculiar shape in the low-density region. This may be explained as the effect of a strong radial corona along the leader channel caused by the pre-existing space charge originating from the negative electrode (Fig. 37*a*) (see Part 4 of the paper).

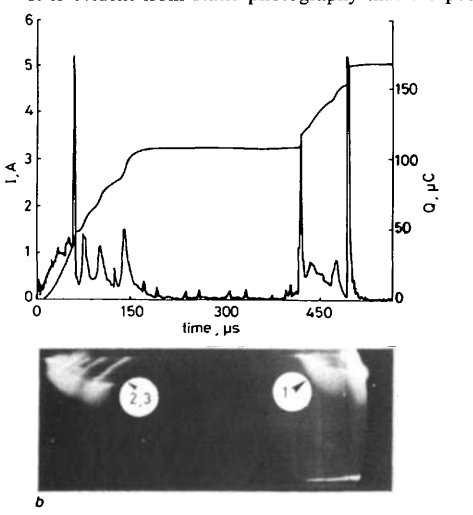

Fig. 36 *(a) Records of current/charge for the shot illustrated in Fig. 35 and (b) record of image convertor*

b { Right part: basic leaders. The weak short leader is covered by the long leader (2, 3)
Left part: reactivation phase of the short basic leader (1) }

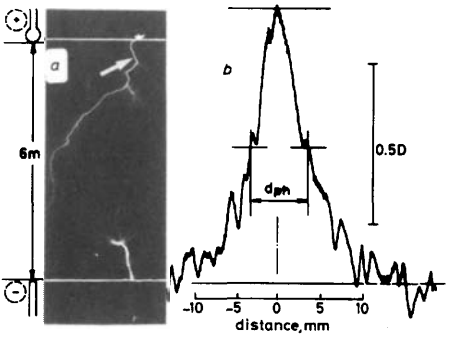

Fig. 37 *Example illustrating discharge channels of different polarity*

a Lower leader: negative leader starting at Δt = 40 000 μs before the positive one (U^- = 2250 kV)
Upper leader: positive leader which propagates into negative space charge
b Typical density profile of a positive leader section during the 'pre-existing space-charge' experiment (D = image density; real leader radius, mm)

In conclusion, although the photographic recording technique has some limitations, it is considered to be useful for leader diameter measurements, especially in the gap space where schlieren techniques are difficult to apply.

6.3 Characteristics of the leader channel derived from schlieren records using slit-streak technique

P. DOMENS, J. DUPUY, A. GIBERT, F. RÜHLING AND B. HUTZLER

6.3.1 Introduction: The measuring system for obtaining schlieren (strioscopic) records has been described in Part 1. This paper deals with the analysis of the imprints of the leader channel taken in streak mode, which enables the direct measurement of the temporal development of the thermal diameter.

To correlate the leader diameter ϕ to electrical parameters, the most relevant parameters, the current I and the charge Q injected into the gap, have been measured.

The streak-mode refers mainly to the voltage perturbation experiment (Part 3). A part of the results relate to the experiments of the pre-existing space charge (Part 4).

6.3.2 Method of analysis: As the limits of the thermal leader channel are well defined on a schlieren picture, it is possible to measure the leader diameter at any instant by means of a suitable enlargement of the film negative. A higher precision can only be obtained from the measurement of micro-image properties in terms of image density fluctuations. For this purpose the records were analysed by a double beam microdensitometer. A magnification of 50 was used, with 50 mm on the plotting table then being equivalent to 1 mm on the schlieren sample.

The density profile recorded on a 50 ASA negative film exhibits a maximum and a minimum value as illustrated in Fig. 38. These values are related to a ground density level D_0 which corresponds to the exposure by the auxiliary luminous flash source (Part 1). The density profile is

divided into a clear and a dark side, where the separation line displays the location of the leader channel axis. As the

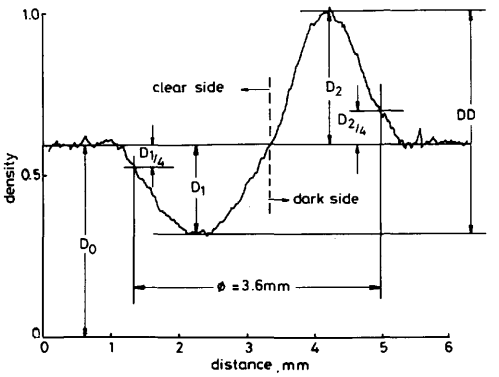

Fig. 38 *Density profile of a schlieren record and definition of the leader diameter ϕ*

off-axis transition to the ground density is not definite, a quarter of the density amplitude has been used for the definition of the limits of the leader channel (Fig. 38).

Besides the measurement of the diameter, the total variation of density $DD = D_1 + D_2$ has been measured as the sum of the positive and the negative amplitude. This density property is considered as being related to the neutral density perturbation inside the leader channel.

6.3.3 Results: The presentation of the results is divided into four sections corresponding to the four phases of the leader growth:

(i) initial phase, lasting a few microseconds
(ii) expansion phase, during current injection
(iii) phase of perturbated expansion
(iv) final jump phase, or (v) zero-current phase, in the case of withstand.

(*i*) *Initial phase:* There is evidence that the inception of the thermal channel of the leader is associated with the emission of a sonic wave. The microdensitometer analysis confirms that there is no density fluctuation before the instant of the sonic wave generation. The sonic wave is clearly detectable during the experiment with pre-existing space charge. Typical schlieren pictures and corresponding increase of the leader cross-section are shown in the paper. If the initial phase of the schlieren record is analysed in detail, the birth of an initial sonic wave is clearly indicated (Fig. 39).

(*ii*) *Expansion phase:* The curves of the leader cross-section as a function of time show a steady increase of the cross-section (Part 3). A linear dependence may be assumed for the main parts of this phase. This behaviour is more justified if the current is flowing continuously. The straight portions of the curve relevant for the expansion phase provide an approximate mean value of 0.1 $m^2 s^{-1}$ for dS/dt, which decays to half this value for later portions of the expansion phase, which is normally associated with a decreasing current. The values are derived from shots obtained from voltage perturbation experiments.

(iii) *Perturbed expansion:* By means of micro-image analysis, it is possible to obtain a reasonable time resolution of about 1 μs for a 200 μs streak schlieren record. This resolution enables the detection of discontinuous leader expansion caused by the application of the second impulse or by the natural reillumination of the leader itself. From the $S(t)$ curves of Fig. 8, the effect of such events can be clearly seen in terms of a fast expansion

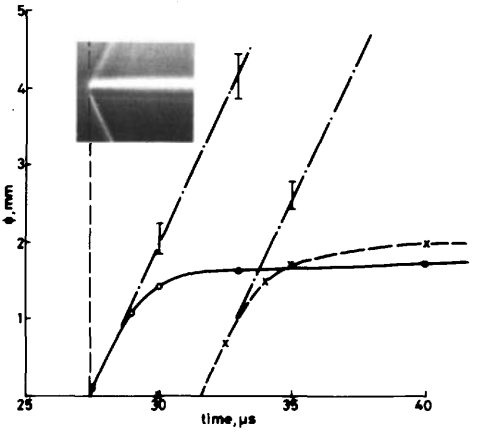

Fig. 39 *Examples of the initial phase of a leader development starting from a sphere electrode (part 4)*

of the channel. The so-called explosion starts with a mean value $S(t) = 0.3$ $m^2 s^{-1}$ which is at least three times higher than the value of the normal expansion phase. The corresponding value of the radial velocity is 310 m/s. If no breakdown occurs the rate of expansion decays to 0.02 $m^2 s^{-1}$ or lower depending on the current, which will have stopped flowing in most cases.

(*iv*) *Final-jump phase:* The transition from the steady expansion of the leader to the final jump may begin with a significant increase of the radial expansion velocity, as illustrated in Fig. 40. The radial velocity increases from

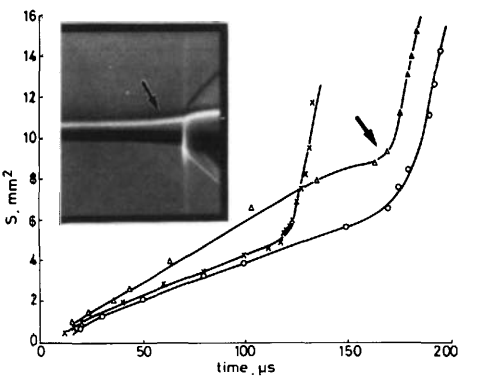

Fig. 40 *Leader section as a function of time for three different breakdown cases*
The photograph illustrates the final jump phase

about 6 m/s to 45 m/s. The continuous expansion dS/dt of 0.02 $m^2 s^{-1}$ increases to 0.5 $m^2 s^{-1}$.

(*v*) *Zero-current phase:* Schlieren pictures show that, even if the current has dropped to zero, the leader channel still expands. This is due to the thermal expansion of the channel into the surrounding air at atmospheric conditions.

The temporal evolution of DD follows the increase of the injected charge (Fig. 41). Whereas the diameter $\phi(t)$ exhibits a step due to the current peak at Δt of 60 μs, the density curve is only slightly influenced by this perturbation. When the current extinguishes in the region of 150 μs,

the DD values start to decrease. To exclude an influence of the flash source, its radiation as a function of time has

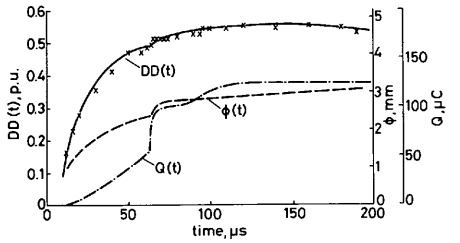

Fig. 41 *Variation of density DD as a function of time with associated temporal development of diameter ϕ and charge Q*
$DD(t) = D_1(t) + D_2(t)$

been analysed. In spite of the fact that the radiation is not fully constant, the density level of the imprint is high enough for the recording of the characteristic maximum and minimum densities.

6.3.4 Discussion and interpretation:

(*a*) *Zero-current phase:* The rate of expansion of the section S of the thermal channel is lower than 0.02 $m^2 s^{-1}$. After a time lag (Fig. 41) the density of the neutral species within the leader is increasing with time. A mass transfer does exist between the leader channel and the external air. Then the mass of the gas contained in the leader channel is no longer a constant.

(*b*) *Initial and perturbed expansion:* For sudden energy inputs there is an explosive mechanism with a local pressure enhancement. A shock wave is then launched as evidenced by the experimental sonic wave. After this explosive mechanism, the local pressure P inside the leader channel returns to a normal value near P_0 (atmospheric pressure). Thus, the expansion of the leader channel takes place with a constant internal mass. Nevertheless, the leader structure is not homogeneous (neutral species distribution presents a minimum on the axis [13]) and this structure is a function of time. The rate of energy transfer f_T from the charged species to the neutral species is also a function of time, with a value about 20 to 30% for a microsecond time interval [13].

(*c*) *Expansion phase:* The energy conservation principle for a given constant internal mass of gas leads to the expression [14]

$$\frac{\gamma}{\gamma - 1} P \frac{dS}{dt} = f_T EI \tag{4}$$

where $\gamma = C_p/C_v$ and E denotes the longitudinal electric field in the leader. For experimental values of:

$$\frac{dS}{dt} = 0.1 \text{ m}^2 \text{ s}^{-1} \quad I = 1 \text{ A} \quad \gamma = 1.4 \quad P = P_0$$

one finds

$$f_T E = 3.5\ 10^4 \text{ V/m}$$

For the initial stage of leader expansion we assume $f_T = 0.3$. Thus one finds

$$E = 1 \text{ kV/cm}$$

This value is consistent with known values from earlier results [10, 14].

For the later leader lifetime we assume $f_T = 1$. Thus $E = 0.35$ kV/cm. This value indicates that the longitudinal electric field near the energised electrode decreases with time, in accordance with a previous formula [15].

6.4 Space-charge distribution and leader channel characteristics

I. GALLIMBERTI AND A. OSGUALDO

6.4.1 Introduction: When a switching surge of positive polarity is applied to a long rod-plane gap, the breakdown process is characterised by the formation and propagation into the gap of a 'streamer-leader' system (Fig. 42): the

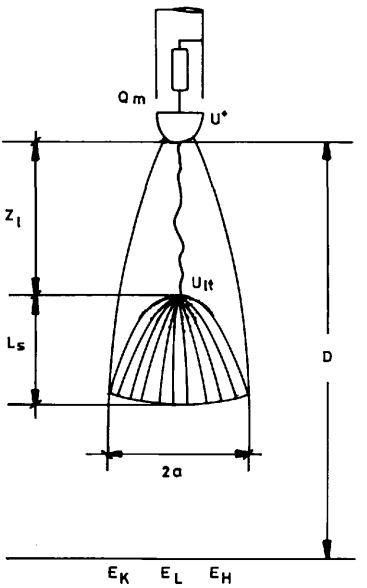

Fig. 42 *Schematic representation of the leader-streamer system*

most important ionisation phenomena occur in the front of the streamer region, supported by the field created by the leader channel and the positive space charge.

The leader channel, a relatively conducting plasma channel, elongates into the leader corona glow, collects the glow current and conducts it towards the HV electrode; however, its resistivity is appreciable and a voltage drop of few kV/cm exists along it.

During the streamer-leader development, electrical measurements (voltage, electric field, conduction or displacement current, charge) can be taken with probes only on the electrode surfaces: therefore, it is possible to study the electrostatic configuration of the leader-streamer system not from direct measurements inside the gap, but only from boundary conditions on equipotential surfaces.

To gain information on the field and potential distributions inside the discharge, it is necessary to assume space-charge and leader-channel models and then try to match the experimental boundary conditions. However, the assumed models are always so simplified that the gained information is generally very poor [9, 16].

In this Appendix a relatively detailed electrostatic model of the streamer-leader system [18, 19] is used to analyse the electrical boundary measurements, together with the time-resolved photographic characteristics. Such an analysis is applied to stable propagation conditions and to perturbed conditions, to estimate the dependence of the streamer-leader characteristics on the discharge parameters and on the stress that is externally applied.

6.4.2 The streamer-leader electrostatic model: The streamer-leader system is schematically represented in Fig. 42: the streamer and the leader extend over a lengths L_s and Z_l, respectively. In the model the discharge is assumed to be rotationally symmetric, and the leader channel is assumed to propagate straight along the gap axis.

To calculate the field at any point in the gap, three different contributions have been taken into account, and their effects have been superimposed:

(*a*) *The electrode-leader system:* This system is formed by the positive rod at a potential U_+, by the negative plane at a potential U_-, and by the leader 'pseudoelectrode', which has a longitudinal voltage drop ΔU_l and a tip potential $U_{lt} = U_+ - \Delta U_l$. The leader pseudoelectrode has been represented with a very slender paraboloid, with a curvature radius at the tip of a few micrometres [17]. First, the purely geometric field, in absence of any leader channel, has been estimated and then the presence of the leader pseudoelectrode has been taken into account. During the present experiment, the application of the same voltage to both electrodes did not result in the same field distribution (Fig. 2, Part 1): the geometric field has been therefore estimated by combining the calculated fields of this Figure.

In Reference 19 it has been shown that the effect of a leader channel on the field distribution in front of the leader head can be represented, with a good approximation, by a weighted combination of the geometric field with the field produced by the leader pseudoelectrode at the potential U_{lt}. The weights depend on the rod curvature radius and on the leader length.

(*b*) *The space-charge region:* The leader corona extends from the leader tip down to the streamer advancing front; however, the space charge lies not only in that region, but also in all the part of the gap that has been crossed by the subsequent coronas; this is a bell-shaped region where the net space charge Q_0 is distributed nonuniformly, with a density increasing near the axis and towards the HV electrode.

Such a kind of distribution has been simulated [18, 19] with a sector of rotational ellipsoid limited by confocal hyperboloidal surfaces: it is geometrically characterised by its length $b = Z_l + L_s$ and by its maximum diameter $2a$ (Fig. 42).

In Reference 19 it has been shown that, if an ellipsoidal-hyperboloidal co-ordinate system is introduced and a uniform charge density is assumed in this frame, the actual density gives results similar to that of the practical case, and the field can be calculated analytically along all the gap.

(*c*) *The induced charges on the electrode surface:* The contribution to the field in the gap, due to the surface charges induced on the plane electrode by the space charge Q_0, can be easily studied by means of the 'image charge' method.

On the contrary, the application of this method to the rod electrode would be approximate and rather complicated: as proposed in Reference 19, if the rod is approximated by a rotational hyperboloid with equivalent curvature radius, the induced charge Q_i can be analytically calculated as a fraction α_i of the space charge Q_0: α_i is called the induction factor, and is a purely geometrical parameter; it depends only on the electrode curvature radius and on the space-charge extension. The field in the gap can be then calculated by assuming an appropriate distribution of Q_i on the rod surface [19].

The charge induced by the space charge Q_0 on the leader pseudoelectrode can be simulated by almost uniformly charged segment [19], which slightly reduces the contribution of the electrode-leader system; this reduction has been neglected in the present calculation.

6.4.3 Analysis of experimental results: The described electrostatic model of the discharge makes it possible to calculate the electric field on the plane electrode, and to compare it with the time-resolved experimental results, if the basic model parameters (Z_l, L_s, a, Q_0, U_+, U_-, U_{lt}) are assigned as functions of time.

The geometric parameters (Z_l, L_s and a), have been derived from the spark-track computer reconstruction (see Fig. 16, Part 1) and from the streak photographs; the value of Z_l can be quite accurate; on the contrary the values of L_s and a are very inaccurate. However, a sensitivity analysis of the computed field values on the plane electrode has indicated that they are not very sensitive to L_s and a variations.

The net space charge Q_0 does not coincide with the measured charge Q_m: in fact Q_m is lower by the charge Q_i on the measuring electrode.

It is therefore

$$Q_0 = \frac{Q_m}{(1 - \alpha_i)} \tag{5}$$

The correction factor depends only on the rod curvature radius and on the space charge extension b: it can therefore be calculated if the geometric parameters are known.

The voltages U_+ and U_- are obviously known as functions of time. The only parameter which could not be measured is the leader tip potential U_{lt}: however, it can be estimated with an iterative procedure to give the best fit of the experimental field values on the plane.

Fig. 43 gives an example of the model application for the optimisation of U_{lt} in the case of both LI and SI voltage perturbation.

In the subsequent rows are presented, respectively, the experimental lengths of the leader Z_l and of the streamer front b, the measured charge Q_m and the corrected net space charge Q_0, the measured field at probe L, the rod potential and the optimised leader tip potential with respect to the plane, and the average field along the leader, calculated as the ratio of ΔU_l to the real leader length L_l, obtained also from spark track reconstruction.

In the left-hand side example (LI perturbation) the streamers reach the plane when the negative voltage is applied; and the space charge is neutralised by a very small fraction; however, the streamer front starts again from a less-advanced position in the gap.

It can be observed that the charge Q_0 is 1.5 to 2 times the measured charge Q_m, the higher values being associated to the smaller space-charge sizes.

The leader tip potential is slightly increasing in the phase of stable propagation, before the application of the negative voltage. Then, for all kinds of perturbations, it follows the rod potential, without any discontinuity in the voltage drop ΔU_l: as a consequence there is no appreciable variation in the leader average field, even if the current increases from a fraction to some tens of amperes.

The average field decreases with time, in a very stable way and as a result is only slightly influenced by the electrical stress applied to the gap. Such a time-decreasing characteristic is consistent with previous estimates [20] and explains the decreasing part of the breakdown-voltage/time-to-crest characteristics (U-curve).

The average field E can be correlated quite well with the leader real length L deduced from spark track reconstruc-

tion (Fig. 44): it indicates that the local field in any section decreases with the age of the section itself.

where S is the leader cross-section, e the electronic charge, v_e the electron drift velocity and μ_e the electron mobility.

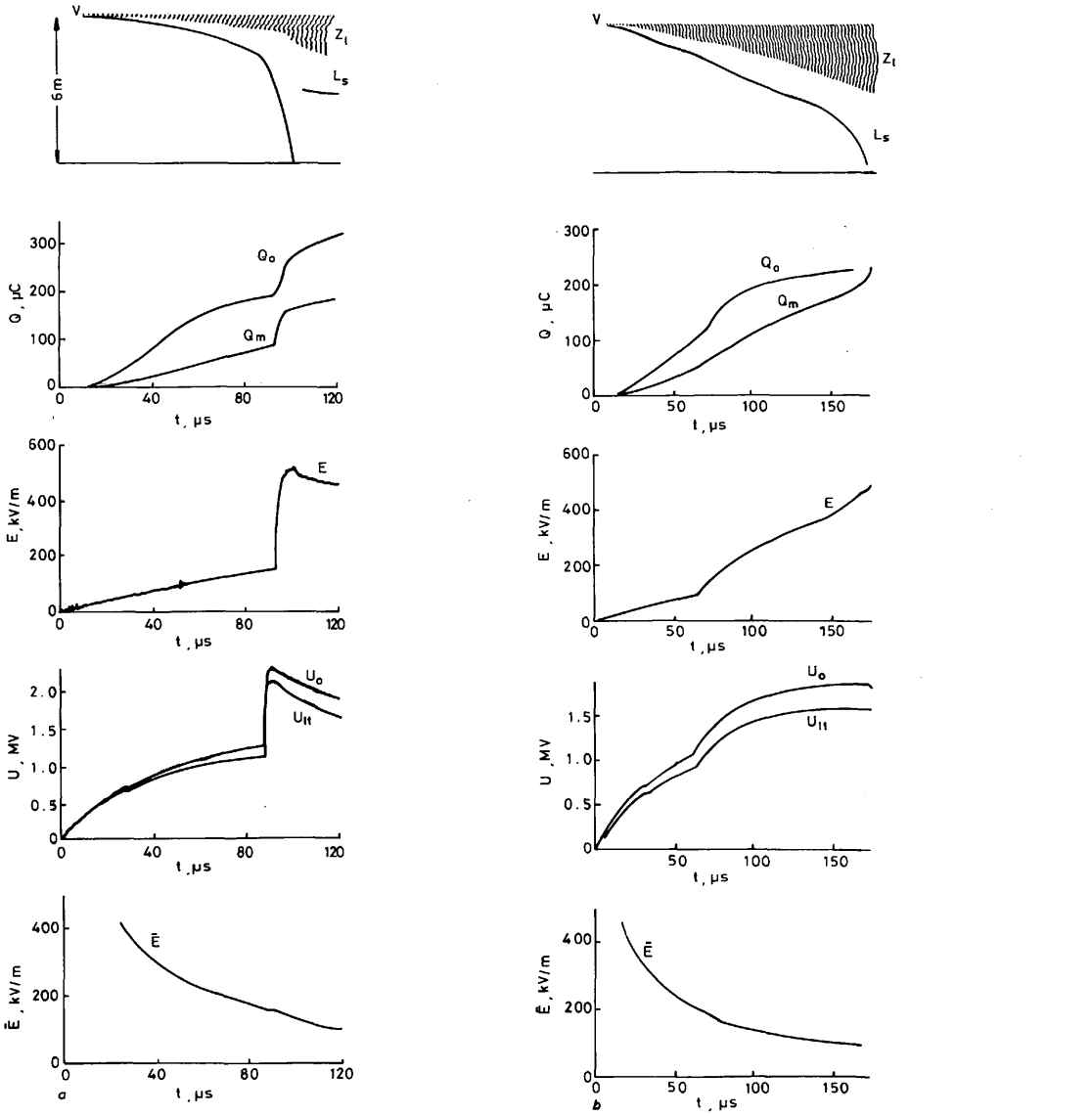

Fig. 43 *Analysis of the leader-streamer propagation characteristics*
a LI voltage perturbation, $\Delta t = 90$ μs; *b* SI voltage perturbation, $\Delta t = 60$ μs.
Row 1: Leader and streamer front advancement
Row 2: Measured charge Q_m and total charge Q_0
Row 3: Measured field at the centre of the plane
Row 4: Applied voltage U_0 and leader tip potential U_{II}
Row 5: Average field $\bar{E}$ along the leader channel

6.4.4 Discussion: The results presented in the preceding section have indicated that the electric field in the leader channel does not change significantly over a wide range of current values. The current depends on both electric field E and electron density n_e

$$I = \int_S n_e e v_e \, dS = e\mu_e E \int_S n_e \, dS \qquad (6)$$

As the field does not change significantly with the current, from eqn. 6 it can be concluded that the electron density within the leader channel varies proportionally to the current. This indicates that there is no local thermodynamic equilibrium (LTE) within the channel: in fact, if LTE would be realised, the ionisation degree and the electron density would be functions only of temperature T and gas number density N (Saha's equation); when a current

peak appears, that lasts for a few μs, T and N cannot vary by a factor 10 in such a short time; furthermore, the temperature cannot decrease when the current decreases.

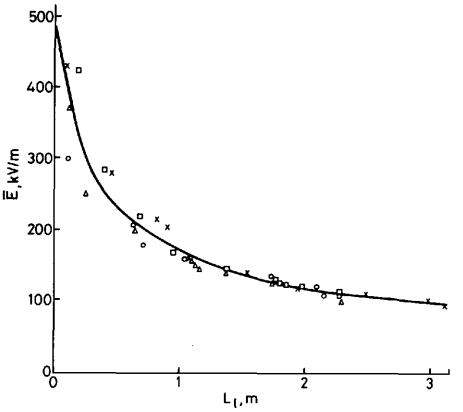

Fig. 44 *Average field $\bar{E}$ as a function of the real leader length L_l*

It is therefore necessary to state that the ionisation in the leader channel is due to a field effect: the electron temperature is much higher than the gas temperature, and supports a high rate of collisional ionisation. When the current decreases the electron density is reduced by dissipative processes: the electron-ion recombination should be fast enough to follow the current variations [17]. Under these conditions the electron continuity equation can be written in the form

$$\frac{\delta n_e}{\delta t} = \alpha n_e v_e - a n_e^2 \tag{7}$$

where α is the ionisation coefficient and a is the recombination coefficient: here the longitudinal variations of n_e are neglected, together with the radial ambipolar diffusion; furthermore, plasma neutrality is assumed within the channel.

Both terms on the right-hand side of eqn. 7 are very large and their difference is very rapidly changing with the reduced field E/N. Under stable conditions ($\delta n_e/\delta t = 0$), the equilibrium electron density is

$$n_e = \frac{\alpha \mu_e E}{a} \tag{8}$$

This is a very steep function of E/N: for $T = 5000$ K and $E = 1$ kV/cm we obtain $E/N = 6.5 \times 10^{-16}$ V cm and $n_e = 5 \times 10^{12}$ cm^{-3}; from this value, n_e can increase by a factor 10 with a change of E/N of the order of 10%. This explains the experimental observations: E/N remains approximately constant in the leader channel, in spite of voltage perturbations and current pulses; however, the absolute field E decreases with time because of the decrease of N due to channel heating and expansion. When a transient perturbation occurs, a slight change in the field gives a large value of $\delta n_e/\delta t$ in eqn. 7 and makes the density n_e follow the current I.

As E varies with time in proportion to the gas number density N, it has to be directly related to the energy input into the leader channel itself. This relationship can be deduced from the present experimental results if the average field $\bar{E}$ is plotted against the measured charge Q_m (Fig. 45): in fact $Q_m(U_+ + U_-)$ represents the total energy delivered by the HV generators.

Let us now consider a generic leader section: the local field E differs from the average field $\bar{E}$; however, if it is

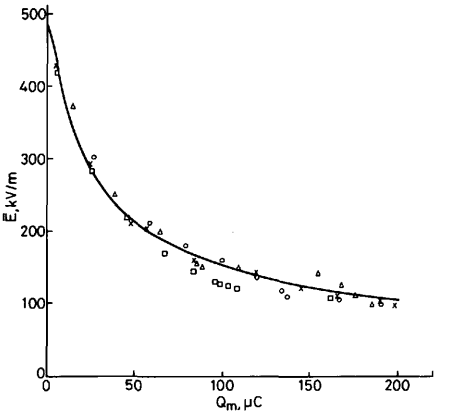

Fig. 45 *Average field $\bar{E}$ as a function of the measured charge Q_m*

assumed that E is a function of the total charge flow through the section, the average field is given by

$$\bar{E}(Q_m) = \frac{1}{Q_m} \int_0^{Q_m} E(Q)\, dQ \tag{9}$$

By differentiation, the local field E can be calculated

$$E(Q_m) = \bar{E}(Q_m) - Q_m \frac{\delta \bar{E}}{\delta Q_m} \tag{10}$$

In Fig. 46 the dependence of the local field E on the charge flow through the leader section is compared with the

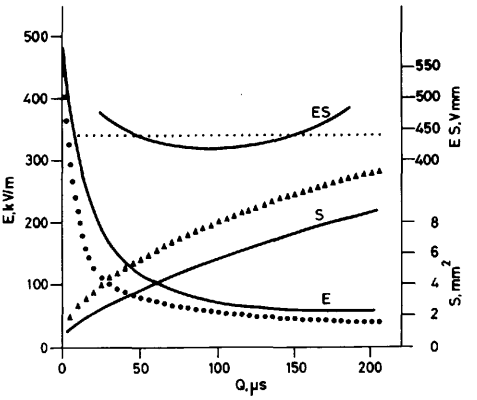

Fig. 46 *Actual leader gradient E and cross-section S as functions of the charge in the section*
The points represent model calculations [6]

dependence of the leader cross-section on that charge, experimentally determined from schlieren records (Fig. 14). The product $E(Q) \cdot S(Q)$ is almost constant: as E/N is also constant, it follows that the product $S \cdot N$, which represents the mass within the channel section, remains approximately constant during the channel expansion.

The results derived in Fig. 46 have been compared with the corresponding values predicted by the non-LTE leader thermodynamic model presented in Reference 17, and the agreement is very satisfactory. They have been also com-

pared with the simplified model presented in a previous Les Renardières Group publication [20]. In this model direct relations have been derived between the leader cross-section, the longitudinal gradient and the charge:

$$S = \sqrt{\left(S_0^2 + 2\frac{\gamma - 1}{\gamma}\frac{E}{N}\frac{S_0}{KT_0}Q\right)} \tag{7}$$

$$E = \frac{E}{N}\frac{N_0}{\sqrt{\left(1 + 2\frac{\gamma - 1}{\gamma}\frac{E}{N}\frac{Q}{KT_0S_0}\right)}} \tag{8}$$

where γ is the ratio between the specific heats, p the pressure, and T_0 and S_0 the values of leader temperature and cross-section at the moment of its formation.

The value of E/N in the model depends slightly on the current: it varies from 5×10^{-16} to 1×10^{-15} for currents ranging from 0.1 to 100 A.

The computed results are reported in Fig. 46 for $S_0 = 1$ mm^2, $T_0 = 1000$ K and $E/N = 6 \times 10^{-16}$ V cm. The section S and the electric field E vary a little faster than the experimental observations, but the general trend and the values of the product $E \cdot S$ are in excellent agreement with those deduced from the experiment.

6.4.5 Conclusions: The use of an electrostatic model of the streamer-leader system has made it possible to derive the leader tip potential and the average field along the channel. The tip potential increases slightly during the stable propagation, and follows the applied voltage during the perturbations; the average electric field, on the contrary decreases with time, and is not significantly affected by perturbations or current pulses.

The discussion of the results has illustrated some interesting characteristics of the leader channel:

(i) no LTE is achieved within the channel

(ii) the ionisation is associated with field effects rather than with thermal effects

(iii) equilibrium between ionisation and recombination defines the electron density within the channel

(iv) during the leader expansion, the mass within the channel remains approximately constant, so that the density is inversely proportional to the section

(v) the reduced field E/N is also approximately constant, so that the field remains directly proportional to the density and inversely proportional to the section

(vi) a decreasing characteristic of leader gradient against charge (associated with leader expansion) is obtained, that is consistent with the U-curves and the saturated breakdown characteristics of long gaps.

All these leader characteristics confirm those assumed or predicted by non-LTE thermodynamic models of the leader development that have been proposed in recent years [17, 20].

6.5 Model of streamer-leader development under voltage perturbation

I. GALLIMBERTI AND E. POLI

6.5.1 Introduction: In the Les Renardières experiments [9, 16] it has been observed that the discharge of long airgaps under positive switching surges is associated with the propagation into the gap of a streamer-leader system (Fig. 42). The streamer ionisation front feeds an electronic current into the leader-corona glow; this current is collected by the leader head and gives the necessary energy input for the head advancement [17]. In turn, the propagation of the relatively conducting leader channel sustains the field at the boundary of the leader corona and supports the activity and the advancement of the ionisation front.

Under switching surges, the streamer-leader system reaches a stable propagation condition, which seems to be essentially related to the voltage rate of rise. It has been suggested that the minimum breakdown voltage in the U-curve, which is associated with the critical front duration, derives from the establishment of optimum conditions for the stable propagation of the streamer-leader system.

In the present experiment it has been shown that the streamer-leader system, propagating under stable conditions, reacts in different ways to a perturbation of the applied voltage, depending on the form of the perturbation and on the time at which it is applied. For lightning type perturbations (short duration transients), three types of reactions have been observed:

(*a*) When the LI surge is applied in the early stages of the discharge progression, the reaction is very small and the streamer-leader propagation is rapidly stabilised leading to the normal unperturbed behaviour; the breakdown probability and times are unchanged.

(*b*) When the LI surge is applied in intermediate stages, the reaction is very marked. The leader corona is strongly enhanced, the leader advances in a rapid jump, but then the discharge extinguishes and does not restart, even if the streamers reach the opposite electrode. The breakdown probability goes to zero.

(*c*) When the LI perturbation is applied on later stages, the discharge is significantly accelerated and develops rapidly to the final jump. In this case, the breakdown probability raises again, and the breakdown times become shorter.

For switching surge perturbations (long duration transients), the reaction of the streamer-leader system is not so marked. The application of the perturbation accelerates the development of the discharge, the acceleration being smaller in the earlier stages of development.

If a positive switching surge is applied to the plane, decreasing the actual potential difference between the electrodes, the discharge is always choked and stops any further development.

In this Appendix a model of the streamer-leader system is described which has been used to simulate the stable propagation of the discharge [18, 21]. This model is then applied to perturbed voltage conditions, for both LI and SI transients, to verify to which extent it can represent the streamer-leader reactions.

6.5.2 The simulation model: The present model of the streamer-leader system makes use of simplified formulations of more sophisticated physical models of single discharge phases. The simplifications that have been introduced lead to a completely analytical formulation, whose basic equations are given in Table 2. The flowchart of the model is reported in Fig. 47: it is organised into four interrelated sections, which correspond to the four groups of equations in Table 2. In the first, the field and potential distributions into the gap are calculated and the field at the streamer ionisation front is derived; in the second, reproduction and the advancement of the streamer heads is simulated; in the third, the current and charge injected in the leader tip are calculated; and, in the fourth, the leader advancement characteristics are derived.

(*a*) *Field and potential distributions:* An electrostatic model of the streamer-leader system has been proposed [18, 19], which makes it possible to calculate potential and

Table 2: The basic equations

List of symbols

Physical parameters
η = attachment coefficient
D_s = thickness of streamer heads
h = absolute humidity
N = gas number density
N_s = number of positive ions

Length, velocity and acceleration
α_1, α_2 = streamer-acceleration coefficients
a_s = streamer acceleration
D = gap length
L_s = streamer length
V_e = electron velocity
V_L = leader velocity
V_s = streamer velocity
Z_l = leader length

Charge, potential, field and current
A, B = HV-rod and leader-tip coefficients
C, C_l = space-charge and induced-charge coefficients
E = field in the leader plasma
E_{gs} = geometric field at the streamer front
$\langle E_g \rangle$ = average field on the electron mean free path for attachment
E_s = total field at the streamer front
I_l = leader current
Q = leader charge
q_l = leader charge per unit length
U_0 = HV-rod potential
ΔU_l = potential drop along the leader
U_{lt} = leader tip potential
U_s = potential at the streamer front

Equations

(i) $U_s = A(Z_s)U_0 + B(Z_s)U_{lt} + [C(Z_s) + C_l(Z_s)]Q$

(ii) $E_s = \frac{\partial}{\partial Z} U_s$

(iii) $U_{lt} = U_0 - \Delta U_l$

(iv) $\Delta U_l = 1.407 \frac{Z_l}{Q}\left[\sqrt{\left(1 + 1.04 \times 10^{25} \frac{E}{N}(Q-1)\right)}\right]$

(v) $\frac{dN_s}{dt} = \frac{N_s V_s}{U_s}\left[E_s - \frac{49 - 0.243 \times 10^{-5} E_s}{D_s}\right]$

(vi) $a_s = \frac{dV_s}{dt} = \alpha_1 \frac{dN_s}{dt} + \alpha_2 \frac{dE_s}{dZ} V_s$

(vii) $I_l = eN_s(V_s - V_l)\frac{E_{gs}}{U_{lt}} + \frac{eN_s}{D_s \eta}(V_e + V_l)[1 - \exp(-\eta L_s)]\frac{\langle E_g \rangle}{U_{lt}}$

(viii) $Q = \int_0^t I_l \, dt$

(ix) $V_l = \frac{I_l}{q_l}$

(x) $q_l = \frac{6}{U_{lt}\left[1 + 1.25 \times 10^3 \frac{h}{V_l}\right]} \times \log_{10} \sqrt{\left[\frac{(D - Z_l)}{1.25 \times 10^6}\right]}$

(MKS units)

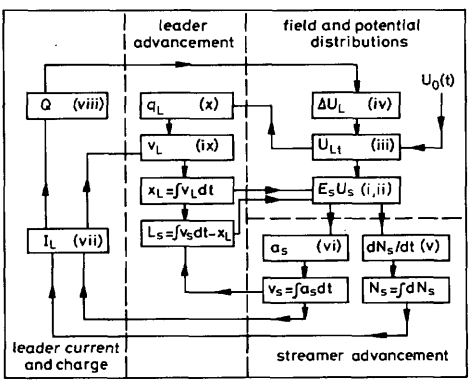

Fig. 47 *Flow-chart of the leader-streamer advancement*

field along the gap in a completely analytical form. In the present model, it is necessary to calculate the leader tip potential U_{lt}, the potential U_s and the field E_s in the streamer front, which guide the streamer propagation.

In Reference 19 it has been shown that the potential U_s and field E_s at point $Z_s = D - Z_L - L_s$, which appear as the externally applied potential and field to the propagating streamer heads, result from the superposition of the contributions of electrodes, leader channel, space charge and induced charges (eqns. i and ii). $A(Z_s)$ and $B(Z_s)$ represent the contributions to the local potential, respectively, of the HV rod and of the leader channel, per unit potential; $C(Z_s)$ and $C_l(Z_s)$ represent the contributions, respectively, of the space charge and of the induced charges, per unit charge. The analytical form of these different contributions is reported in Reference 19.

The leader tip potential can be derived from the applied voltage U_0 if the voltage drop ΔU_l along the leader channel is known (eqn. iii).

The analysis of the experimental results, by use of the same electrostatic model of the streamer-leader system, presented in Appendix 6.4, has shown that the leader gradient is a decreasing function of the charge flow into the channel, because of the thermodynamic phenomena which cause an expansion of the channel itself. These results are in very good agreement with the predictions of non-LTE thermodynamic models of the leader channel which have been recently proposed [17, 20]. In the present case, reference has been made to a simplified model [20] which has the advantages of a completely analytical formulation: it gives the voltage drop ΔU_l as a function of the leader length Z_l and of the injected charge Q (eqn. iv).

(*b*) *Streamer advancement:* A streamer model has been developed [22, 23], which makes it possible to simulate the propagation of a single streamer if the externally applied field is known. The streamer head is represented as a sphere of diameter D_s containing N_s positive ions, in front of which develops a series of secondary avalanches originated by photoelectrons; the electrons of the secondary avalanches neutralise the positive charge of the streamer head and leave a track of positive ions, which represents the new streamer head in a more advanced position in the gap.

The streamer propagation results from a series of elementary steps of this type, each of them governed by an energy conservation equation.

A similar cumulative equation (eqn. v) has been used for the sheet of streamer heads which forms the front of the leader corona. In this case, N_s represents the total streamer front charge, D_s the thickness.

In Reference 21 it has been shown that the streamer velocity V_s depends essentially on the local field in which the secondary avalanches develop, which is partly due to the externally applied field, partly to the field of the head positive charge. The velocity V_s therefore increases almost proportionally to a linear combination of E_s and N_s.

A similar linear relation (eqn. vi) has been used in the

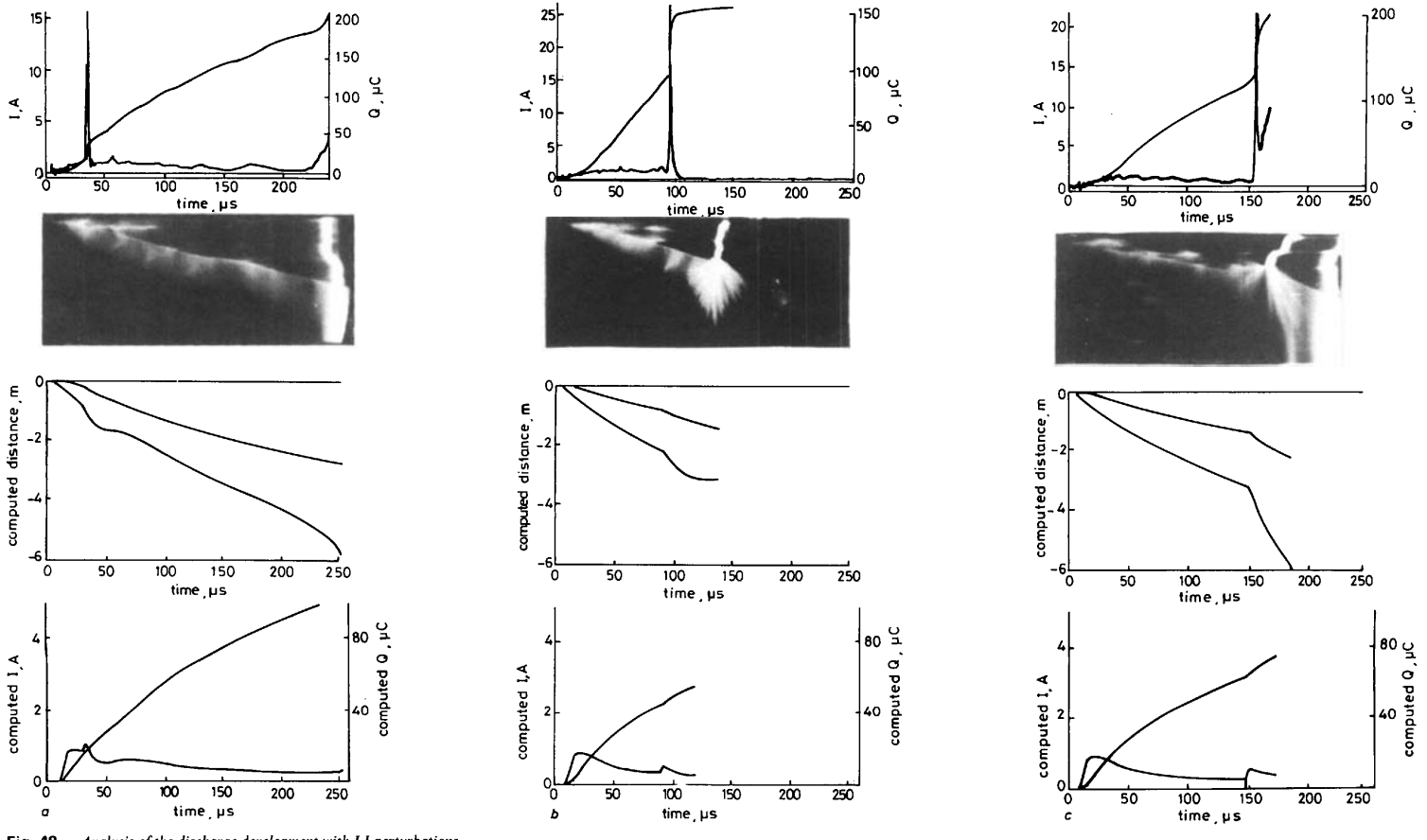

Fig. 48 *Analysis of the discharge development with LI perturbations*
$U_- = -0.8$ MV: (*a*) $\Delta t = 30\ \mu s$, (*b*) $\Delta t = 90\ \mu s$, (*c*) $\Delta t = 150\ \mu s$
Row 1: Measured current and charge Row 2: Image convertor photograph Row 3: Computed development of the streamer-leader system Row 4: Computed current and charge

present model for the streamer acceleration. The coefficients α_1 and α_2 have been estimated according to the results reported in Reference 23.

(*c*) *Leader current and charge:* To calculate the current input in the leader tip, let us assume a reference frame moving into the gap with the same velocity V_L as the leader channel.

For the leader channel, the moving charges are represented by the N_s positive ions of the streamer front advancing with a relative velocity $V_s - V_l$, and by the corresponding electrons moving in the glow region with a relative velocity $V_e + V_l$ towards the leader tip.

The positive-ion current component can be easily calculated, as the positive ions are localised in a very thin region: it is given by the first term in eqn. vii, where E_{gs} is the geometric field produced in the streamer front by the leader tip at potential U_{lt} and by the rod at potential U_0.

The electron current component has to be integrated in the whole glow region, taking into account that the electron number decays exponentially towards the leader tip because of attachment. It is given by the second term in eqn. vii, where $\langle E_g \rangle$ represents the average geometric field produced by the leader tip and the rod over a distance $1/\eta$ behind the streamer front (which represents the electron mean free path for attachment).

The total charge which has flowed into the leader tip is obtained by integration of I_l (eqn. viii).

(*d*) *Leader advancement:* A leader head model has been developed [17] which makes it possible to simulate the leader propagation, if the current I_l that feeds its tip is known. In this model, the leader head is represented as a slender paraboloidal surface, across which a jump in conductivity is present, from the low value of the corona glow to the high value of the leader channel. Such a jump in conductivity is assumed to be caused by the detachment of negative ions (under the combined action of field and gas temperature), which liberates a large number of free electrons.

In the model, the current and field distributions in front of the leader channel are calculated and the energy transfer and relaxation processes under nonequilibrium thermodynamic conditions are simulated, to compute the rate of electron detachment in the transition region where the conductivity jump exists.

The leader advancement velocity is proportional to the leader current (eqn. ix), through a constant q_l (eqn. x), which represents the charge per unit length necessary to realise adequate conditions for the conductivity jump and for the leader propagation.

In eqn. x all the variables have to be expressed in MKS units.

6.5.3 Computed results: The model has been applied to the simulation of the leader propagation, under the experimental conditions used in the tests, on the effect of voltage perturbation.

(*a*) *Lightning impulse perturbations:* For LI perturbations the three cases of different leader reactions ($\Delta t = 30$, 90 and 150 μs, respectively) are reported in Fig. 48, for a negative crest voltage $U_- = -800$ kV. In all cases, the sharp lightning impulse produces a transient increase in the leader tip potential U_{lt} and hence of the field on the streamer heads E_s; this causes an acceleration of the advancing streamer front and a consequent increase of streamer length (Fig. 48). At the same time, the increase of the geometric fields E_{gs} and $\langle E_s \rangle$ leads to a rise in the current I_l that feeds the leader tip and to an increase of its advancement velocity.

The size of this change of the leader-streamer propagation characteristics depends on the time at which the perturbation is applied.

For $\Delta t = 30$ μs the space charge and the leader conductivity are relatively small and the change in the propagation characteristics is limited: as the streamer front elongates far from the leader tip the field E_s is reduced and the streamer velocity decreases. The leader channel advancement velocity is not affected immediately by the reduction of the streamer activity, because the electronic component of the current I_l decays slowly with the attachment time constant. Owing to this fact and to the relatively high rate of rise of the applied positive voltage U_+, the fields E_s, E_{gs} and $\langle E_g \rangle$ are rapidly restored to the values of normal propagation and the leader-streamer system recovers stable advancement conditions (Fig. 48*a*). After the short transient perturbation, the discharge continues to propagate as in the unperturbed case. The breakdown probability is not significantly affected, and the breakdown times remain almost unchanged.

For $\Delta t = 90$ μs, the space charge and the leader conductivity are higher and the change in the propagation characteristics becomes larger. The streamer elongation leads to a more significant reduction of the field E_s and of the streamer velocity V_s. In this case, the rate of rise of the positive voltage U_+ is much smaller, so that the fields E_s, E_{gs} and $\langle E_g \rangle$ cannot recover fast enough and the streamers continue to decelerate until they stop. After a few microseconds the electronic component of I_l extinguishes and also the leader stops (Fig. 48*b*).

For $\Delta t = 150$ μs the propagation of the leader-streamer system is mainly governed by the space-charge field, which gives the major contribution to E_s [6]. When approaching the opposite electrode, the contribution of the image charge in the plane is added, and the field E_s rapidly increases. For this reason the sharp elongation of the streamers after the application of the perturbation does not lead to a decrease of the field E_s. The streamer velocity increases near the plane (Fig. 48*c*), and the final jump follows when the streamers reach it.

In this case, the discharge evolution is accelerated, and the breakdown times are shortened. However, also, for $\Delta t = 150$ μs withstands of the gap can occur for leaders with an oblique path that reach a relatively short axial length at the time when the voltage perturbation is applied. This can be simulated in the model by introducing a tortuosity coefficient [17]. In this case, the same behaviour as in Fig. 48*b* is obtained.

The simulation model can reproduce quite well the leader-streamer advancement characteristics when LI voltage perturbations are applied; also the average values of current and charge are consistent with those experimentally observed (Fig. 48). However, the amplitude of the current pulse that follows the application of the perturbation is very much different. This is probably due to the fact that in the real case a new corona develops from the leader tip, which overlaps the existing corona glow and injects a large charge into the leader channel (Fig. 48*b*). This is not simulated in the present model, but it could be simulated by an appropriate increase of the space charge Q and of the number of positive ions N_s in the streamer front. However, as the model results reproduce fairly well the leader-streamer reactions that have been experimentally observed, it can be assumed that the new corona does not change the propagation mechanism, but only influences the charge distribution of the pre-existing leader corona.

(*b*) *SI perturbations:* For SI perturbations, two cases

are presented in Fig. 49, namely, $\Delta t = 60$ μs, $U_- = -0.45$ MV, and $\Delta t = 120$ μs, $U_- = -1.0$ MV. In the first behaviour is observed, but with much larger variations of leader and streamer velocities (Fig. 49*b*). Owing to the fact

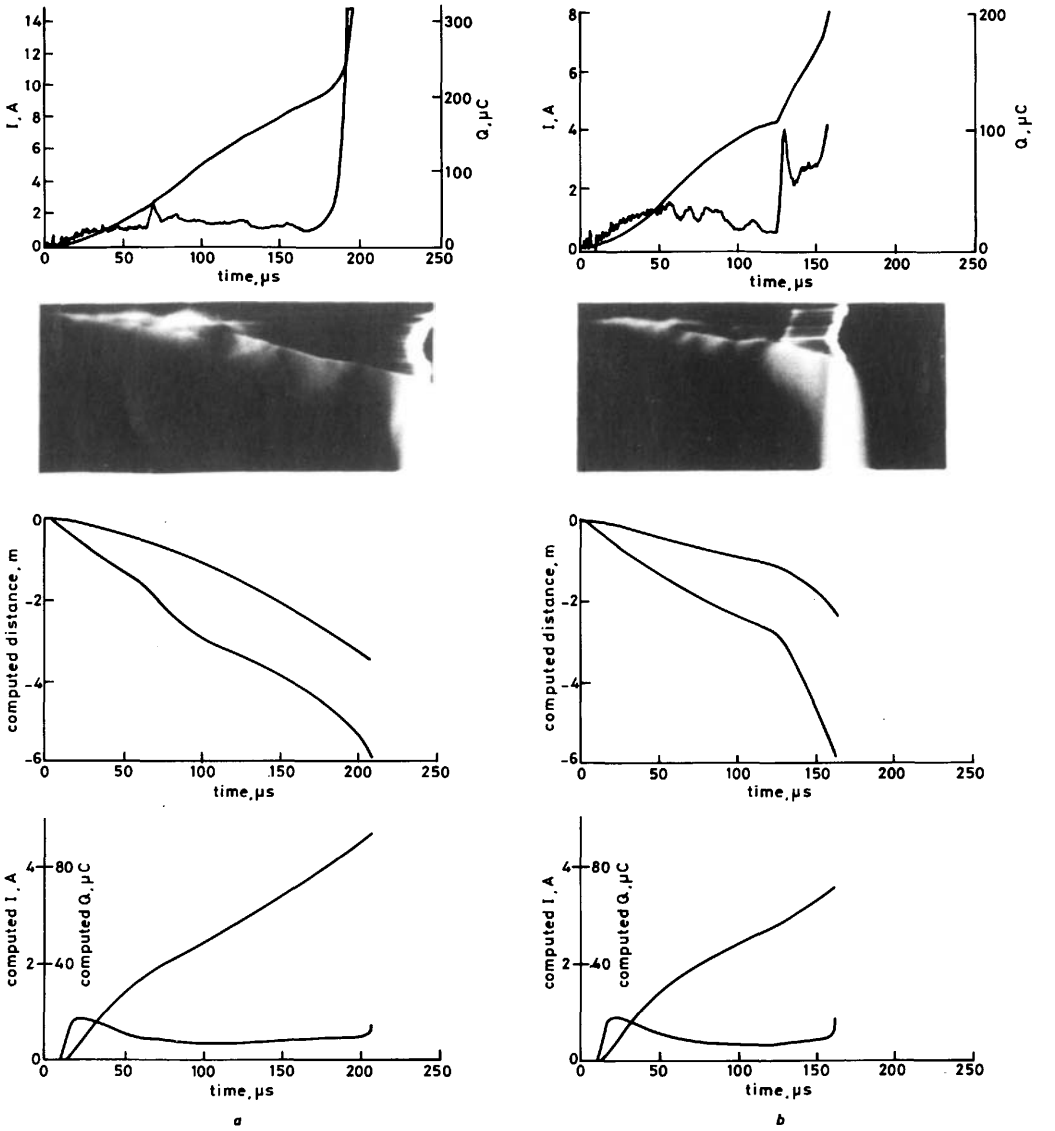

Fig. 49 *Analysis of the discharge development with SI perturbations*
(a) Δt = 60 μs, (b) Δt = 120 μs
Row 1: Measured current and charge
Row 2: Image convertor photograph
Row 3: Computed development of the streamer-leader system
Row 4: Computed current and charge

case, the impulse application increases the field E_s and accelerates the advancement of the streamer front. Also the fields E_{gs} and $\langle E_g \rangle$ increase, leading to a higher leader current I_l and velocity V_l. Owing to the relatively slow rise time of the perturbation voltage, the leader-streamer system reaches new equilibrium conditions with a larger streamer length and a higher leader current and velocity (Fig. 49*a*). This new régime of propagation always leads to breakdown, with a slightly smaller time to breakdown.

In the case of $\Delta t = 120$ μs, $U_- = -1.0$ MV, a similar that, under these conditions, the propagation of the leader-streamer system is essentially governed by the space-charge field, the streamer propagation is continuously accelerated until the streamer front reaches the plane. Also for the SI case, the average current and charge values are consistent with the experimental observations, but the changes predicted for the perturbation application are smaller than the observed ones.

During the experimental test period, the effects of the crest voltage of the perturbation on the leader-streamer

propagation were studied. The model has therefore been used to predict the dependence of the leader velocity on the voltage rate of rise, and of the breakdown times on the crest voltage. The comparison between computed values and experimental results (Figs. 50 and 51, respectively) shows excellent agreement.

The last type of voltage perturbation which was investigated in the experimental test period was the case of partial chopping, when two positive voltages are applied to both electrodes. The simulation of one of these cases is reported in Fig. 52, for $\Delta t = 120$ μs and $U_- = -0.45$ MV.

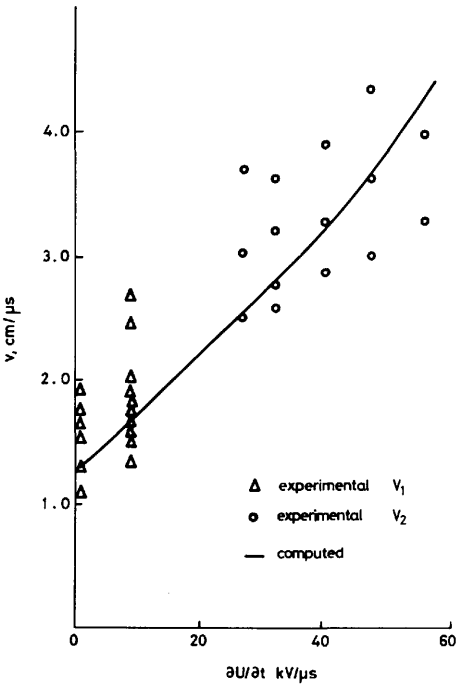

Fig. 50 *Measured and computed leader velocity before (V_1) and after (V_2) SI application as functions of the rate of rise of applied voltage*

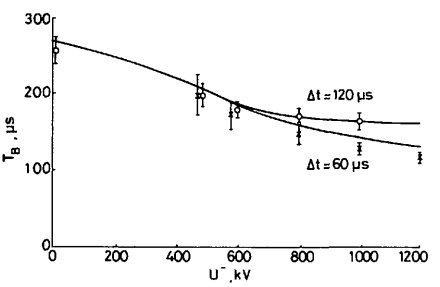

Fig. 51 *Measured and computed time to breakdown T_b as a function of U^- with SI perturbations for two different values of Δt*

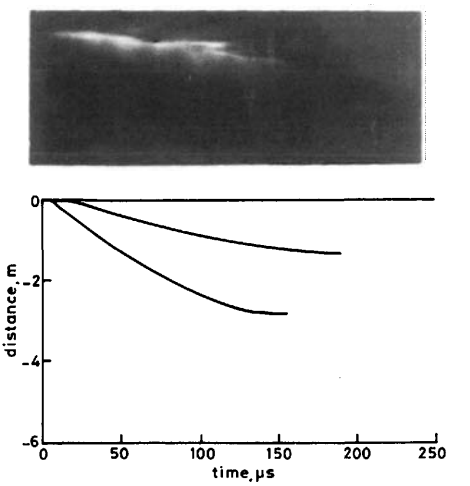

Fig. 52 *The discharge development with a choking impulse ($\Delta t = 120$ μs, $U_- = -0.45$ MV)*

Row 1: Image convertor photograph
Row 2: Computed development of the streamer-leader system

At the time when the perturbation is applied, the streamer propagation suddenly stops, due to the drop of the field E_s. The leader advancement, however, continues for a short time, owing to the delay in the extinction of the electronic component of the current I_1. This appears to be consistent with the experimental observations, which show an exponential tail in the current record and a short leader head advancement after the streamers have disappeared.

6.5.4 Conclusions: The proposed model of the development of the streamer-leader system is based on the simplified simulation of the different discharge phases. It is completely analytical and can be implemented on small personal computers.

It represents fairly well the stable propagation of the streamer-leader system and its reactions to all types of voltage perturbation applied during the experimental tests. The computed current and charge have consistent average values, but the big pulses associated with LI perturbation do not appear, probably because, in the real case, they are associated with new coronas developing from the leader tip.

Times to breakdown and leader advancement velocities are also satisfactorily simulated for different voltage rates of rise.